



UWB dual-port self-decoupled o-shaped monopole MIMO antenna with small-size easily extendable design and high diversity performance for millimeter-wave 5G applications

Asma Khabba¹ · Jamal Amadid¹ · Sraddhanjali Mohapatra² · Zakaria El Ouadi¹ · Sarosh Ahmad³ · Saida Ibnyaich¹ · Abdelouhab Zeroual¹

Received: 23 January 2022 / Accepted: 18 July 2022 / Published online: 1 August 2022
© The Author(s), under exclusive licence to Springer-Verlag GmbH, DE part of Springer Nature 2022

Abstract

The millimeter-wave spectrum is deemed as an attractive solution to deal with the urgency of the high-data-rate needed to construct the 5G technology systems. Accordingly, this research work presents a high-isolation ultra-wideband dual-port MIMO antenna, and operates at the pioneer 28 GHz band for millimeter-wave 5G applications. The individual antenna consists of a new ring-shaped monopole antenna built on the low loss Rogers RT Duroid 5880 laminate, well-refined to bear a large bandwidth of 10 GHz from 24 to 34 GHz with suitable radiation features including a high radiation efficiency up to 99% and good comparable gain reaches to 5.9 dB. The single-antenna unit is carefully investigated, then exploited to propose a compact orthogonally placed two-port MIMO antenna with small total volume of $11 \times 20.5 \times 0.254 \text{ mm}^3$ while provides a strong isolation surpassing 25 dB. The MIMO diversity performance has been neatly evaluated in terms of various essential metrics, where an impressive performance has been proven. The simulation results are experimentally validated for both single and MIMO structures where a great harmony is demonstrated. Moreover, the impact of connected ground plane scheme on the MIMO antenna performance is also discussed, where a gratifying outcomes are accomplished. Besides, the proposed two-element MIMO antenna is further extended to four and eight elements MIMO antennas with connected ground plane configuration. A pretty simple decoupling structures are used, whereas a very satisfying results are fulfilled. The achieved outcomes make the proposed design superior to many existing designs and highly fit for the 5G wireless systems.

Keywords Ring-shaped antenna · UWB · 5G technology · MIMO antenna · Millimeter-wave spectrum · Strong isolation · 28 GHz band

1 Introduction

In the latest years, the telecommunication industry has devoted considerable attention and effort to develop the new 5G technology. This development is necessary to handle the pressing need for very high throughput and wide bandwidth

to keep pace with the fast and nonstop increase in worldwide mobile traffic [1]. Indeed, the limited potentials provided by the current generation (4G) will not be able to support the modern data-hungry versatile interchanges. Moreover, the 4G is considered insufficient to bring any further upgrades to the mobile communication field, thus necessitating moving on to a new generation with superior capabilities [1, 2]. The fifth generation (5G) is counted as a promising solution for users to reach a colossal data rate of multi-Gigabits-per-second with ultra-low latency, high security, reliability, and high-speed connectivity with massive connected devices density up to one million per Km^2 [2–4]. In addition, the execution of the 5G infrastructure will emerge several advanced technologies such as smart cities, smart agriculture, Smart Gaming, 3D live video, device-to-device (D2D), cloud services, and enormous machine-to-machine communication for industrial automation, vehicular communication,

✉ Asma Khabba
asma.khabba@edu.uca.ac.ma

¹ Instrumentation, Signals and Physical Systems (I2SP) Team, Faculty of Sciences Semlalia, Cadi Ayyad University, Marrakech, Morocco

² Applied RF Research Laboratory, School of Electronics Engineering, KIIT Deemed to Be University, Bhubaneswar 751024, India

³ Department of Signal Theory and Communications, Universidad Carlos III de Madrid, 28911 Leganés, Spain

autonomous driving, and medical services remoting. [5, 6]. Therefore, to realize such advanced futuristic data-hungry applications, the employment of multi-input multi-output (MIMO) antennas with large band property is inevitable for the 5G systems execution. The MIMO system is an efficient technology to enhance channel capacity and improve spectrum efficiency as multiple antennas involve simultaneously in the transmission process, which leads to reliable communication without boosting the input power [7]. Meanwhile, the usage of MIMO antennas sheds light on some practical challenges that should be considered seriously, including the simple antenna design to smooth its integration into MIMO structure besides the compact and small geometry to ease its incorporation into mobile cellular devices. Moreover, the high mutual coupling between closely spaced elements in the MIMO antenna system is a critical problem to be addressed without compromising the overall size, which is beneficial to fit the limited area designated for antenna placement in wireless devices [8, 9]. The International Telecommunication Union (ITU) and the Federal Communication Commission (FCC) have first-ever targeted the millimeter-wave spectrum 24–300 GHz for 5G bands standardization. Indeed, the centimeter-wave band is already saturated by the currently used networks and theoretically attained its maximal exploitation where the bandwidth left is not sufficient for further advancement beyond the fourth generation (4G). The abundantly available bandwidth at the mm-wave spectrum has attracted scientists as an effective solution to solve the bandwidth scarcity issue and accomplish the 5G expectations, including the fast speed and high channel capacity [10, 11]. Furthermore, the utilization of mm-wave frequencies will inherently result in smaller antenna dimensions. Then, multiple antenna elements can be placed in a limited space while keeping high isolation. [11]. However, millimeter-wave frequency signals are hypersensitive to the weather conditions and experience a high propagation loss, where they can resist for just a couple of miles. Besides, the high-frequency signals suffer from high absorption levels while traversing the different obstacles, which drastically degrades the transmission quality [12]. Nonetheless, many practical scenarios, such as the employment of femto-cell and pico-cell base stations, have been discussed to address these crippling issues. These solutions reduce the cell's area to a typical distance at which the severe absorption losses are not very obvious, which inherently improves the coverage zone of the mm-wave signals [13]. Moreover, the bad atmospheric attenuations can be countered by using high gain antennas [14]. On the other hand, the influence of rain and atmospheric attenuation has been experimentally tested throughout the frequency range 0–400GHz. As a result, the performed study disclosed that the minimum signal distortion is obtained in the range 20–40 GHz, which makes it a promising band to establish the 5G

mm-wave networks [15]. Accordingly, numerous researches have been recently reported in the literature to propose various antenna designs operating within the mentioned band. For instance, in Ref. [1], authors have suggested dual-band MIMO antenna for 27 GHz and 39 GHz bands. The intended design had a good bandwidth property; however, the MIMO performance was studied only in terms of envelope correlation coefficient (ECC). In Ref. [2], a 2×2 millimeter-wave microstrip patch antenna array has been designed for 28GHz applications. The design was featured with small dimensions, while a low bandwidth was achieved, and the MIMO design has not been addressed. Likewise, in Ref. [3], a four-element linear array slot-loaded microstrip patch antenna has been executed at 38 GHz. The array was developed to achieve a maximum gain of 7.8 dB. However, the MIMO assembly has not been considered, whereas the MIMO systems are indispensable for 5G systems. In Ref. [7], a very wideband four-port MIMO antenna has been presented to operate throughout the band 23–40GHz. But, a large area of $80 \times 80\text{mm}^2$ has been occupied. Similarly, in Ref. [9], a four-element MIMO antenna with broadband characteristic 25–37GHz has been performed. However, the suggested structure was marked by a relatively large size of $50.8 \times 12\text{mm}^2$, while only the ECC was analyzed. In Ref. [10], a frequency-reconfigurable folded-slot antenna has been investigated to resonate at 27.95 GHz and 28.65 GHz, respectively. The antenna had suitable dimensions, but complex multilayer structure was adopted and narrow bandwidth was attained. In Ref. [16], dual-band mm-wave antenna has been presented for 28/38GHz applications using modified patch geometry and defected ground structure (DGS). Nevertheless, the operating band was just 0.5/0.7GHz respectively. In Ref. [17], two-element MIMO antenna has been made for the employment at 28 GHz and 38 GHz bands using partial ground plane which helps to bear reasonable bandwidth. However, a weak peak gain has been achieved of only 1.83 dB. In Ref. [18], slot-based two-port MIMO antenna has been carried out with very wide bandwidth and good gain. Nevertheless, the overall area was $53 \times 31.7\text{mm}^2$ which is not suitable for the small wireless devices. In Ref. [19], a multiband dolly-shape millimeter-wave antenna has been revealed for the employment at 24/28GHz, whereas low bandwidth was offered. In Ref. [20], an inverted C-shaped 4×4 MIMO antenna has been modeled to operate along the band 25.5–29.6 GHz with total bandwidth of 3.9 GHz. Although the proposed structure was involving DGS to improve the elements isolation, the minimum isolation achieved was just 10 dB. In Ref. [21], a HP-shape four-port MIMO antenna has been designed at 38.5 GHz with wideband characteristic from 36.83 GHz to 40.0 GHz. Nonetheless, the overall size was $32.5 \times 47.4\text{mm}^2$ which needs to be further reduced. Likewise, in Ref. [22], a quad-element MIMO antenna for dual-band operation at 28/38 GHz has

been developed using an inverted I-shaped slots. The MIMO elements provided a good gain value, while the relatively lower bandwidth and the significant size of $55 \times 110\text{mm}^2$ constituted its limitations. In Ref. [23], a quad-ports dual-band slot antenna has been explored for 28/38/39 GHz applications with a wide bandwidth and maximum gain of 7.2 dB. Nevertheless, the overall structure was limited by its bulky area of $158 \times 78\text{mm}^2$. In Ref. [24], a substrate integrated waveguide SIW-based two-port MIMO antenna has been proposed at 28GHz with a maximum gain of 6.9 dB and total size of $33 \times 27.5\text{mm}^2$. However, the insertion of metallic holes have complicated the structure and the operational band was only 0.4GHz. Given the above review, various constraints have been observed in recently published works, as most of the designs discussed are either constrained by their low bandwidth or large dimensions. In addition, the very low gain, complex structure and high mutual coupling constitute some other important vulnerabilities that have been spotted in some of the mentioned works. All these constraints would impair the antennaperformance and degrade its features and strengths, thus reducing its suitability for 5G systems. Accordingly, there is still a necessity to develop an antenna that would effectively accomplish the essential criteria of small size, simple geometry, large bandwidth, and good gain. Besides the strong performance when assembled in the MIMO structure indispensable for 5G communication systems. Hence, building of such antenna is the main objective of this research. Thus, given its attractive features, i.e., low cost, low profile, lightweight, easiness of fabrication, and assimilation into the small electronic devices, the planar antenna has been adopted to carry out this study. It is most appropriate for modern communication systems [14] and can perform efficiently if smartly modeled.

In this manuscript, a comprehensive investigation of a compact ultra-wideband (UWB) two-port MIMO antenna has been presented. The proposed MIMO antenna resonates at one of the most pioneer 5G bands, namely 28GHz. It bears an ultra-wideband from 24 to 34 GHz, desirable for high data rate applications, while it covers several prominent mm-wave bands. The geometrical layout of the MIMO antenna is characterized by straightforward structure and small dimensions of $11 \times 20.5\text{mm}^2$, allowing its smooth incorporation. The two elements are perpendicularly assembled on the low loss Rogers RT5880 substrate for low mutual coupling consideration. Each element consists of a monopole antenna with O-shaped radiating patch and backed with truncated partial ground plane for wide bandwidth purpose. The MIMO performance has been carefully assessed through various essential parameters, i.e., the diversity gain (DG), the envelope correlation coefficient (ECC), the channel capacity loss (CCL), the total active reflection coefficient (TARC), and the channel capacity (CC). On the other hand, the proposed MIMO

antenna is further upgrade into quad-element and octal-element MIMO antennas. Both expanded configurations involve an efficient decoupling structures to boost their performance, where a quite good functioning is acquired. The benefits of the suggested design can be listed as following: firstly, it features a small dimensions compared the other reported designs. Secondly, it provides a large operational band and maintains a simple shape. Thirdly, it features a high isolation without inserting any decoupling structure, which results in strong MIMO performance. Fourthly, it offers a high radiation efficiency and good comparable gain without introducing any gain improvement technique. Fifthly, it shows a pretty good scalability as the extended four-element and eight-element MIMO antennas show a very convincing findings. The acquired results proved the ability of our design to be a strong candidate for 5G systems. This section allowed the readers to be aware of the fifth-generation era and its corresponding literature. The rest of this study is organized as follows: a detailed study of the single antenna is done in Section 2. Section 3 addresses the MIMO antenna performance and evaluates the diversity parameters. The extended 4×4 and 8×8 MIMO antennas is wisely discussed in Section 4. In Section 5, a careful comparison with the existing works is executed. Finally, Section 6 closes the study.

2 Single-antenna design and performance

2.1 Antenna configuration

Figure 1 reveals the configuration of the suggested millimeter-wave antenna. As shown, the suggested layout consists of a monopole antenna with O-shaped radiating element of outer radius r_1 and inner radius r_2 excited by 50Ω microstrip feed-line of length L_f and width W_f and built on the low loss Rogers RT5880 laminate which possess a loss tangent $\tan\delta$ of 0.0009, a dielectric constant ϵ_r of 2.2, and thickness of 0.254mm. A partial ground plane is employed to back the structure, while a rectangular open-ended slot is graved straight down the feed-line to achieve a good impedance matching. The metallic parts of the antenna are made using 0.035-mm-thick copper. The antenna structure was neatly modeled, simulated, and optimized with the assistance of the commercially available CST microwave studio electromagnetic software where the optimization of each parameter was carefully done to extract the most refined version of the antenna with the sought-after frequency response. The overall design is marked by small total area of $8\text{mm} \times 11\text{mm}$ which allows it to be a highly integrable antenna. The final optimized values of all parameters are given in Table 1.

Fig. 1 Proposed antenna geometry

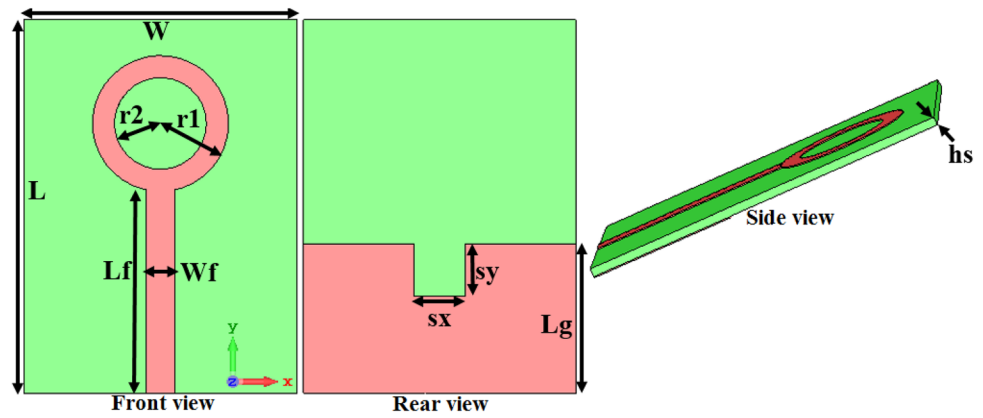


Table 1 Final optimized parameters dimensions

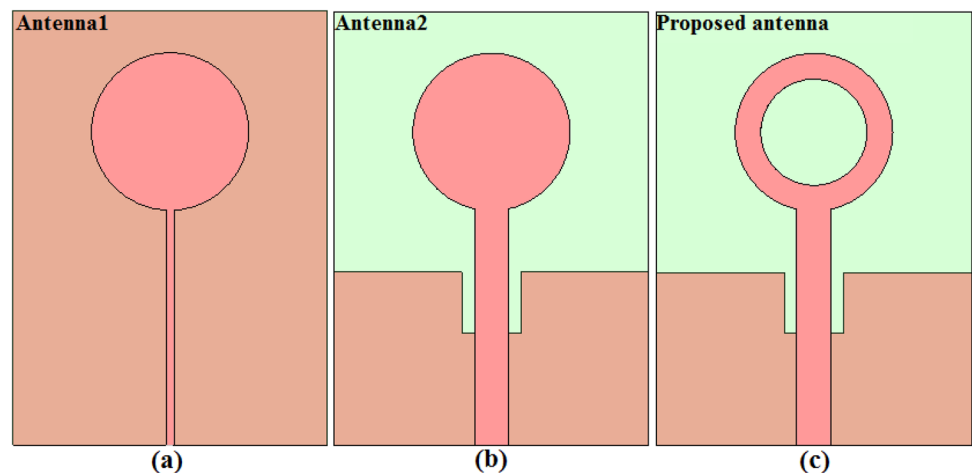
Parameter	Value (mm)	Parameter	Value (mm)
W	8	Lf	6
L	11	Wf	0.87
hs	0.254	Lg	4.4
r1	4	sx	1.52
r2	1.35	sy	1.54

2.2 Evolution procedure of the proposed structure

In an attempt to fully understand the working mechanism of the proposed antenna, Fig. 2 depicts the step-wise geometric design through which the final design has been obtained with the desirable frequency response. As can be noted, the intended design is the modified version derived from the traditional circular patch antenna through three basic phases, where Fig. 3 collects the reflection coefficient obtained in each phase. As shown in Fig. 2a, the design procedure is started by developing a conventional circular microstrip patch antenna (CMPA) named Antenna-1 with full ground plane and full size of

8mm × 11mm × 0.254mm. The conventional antenna was designed to operate at 28 GHz, defined as one of the most important 5G bands, where the radius r1 of the circular radiator was initially determined using the well-known Eqs. (1, 2) [25], while the overall design parameters have been carefully amended inside the CST simulator to get the resonant mode at the desired frequency. As shown in Fig. 3, a fine adjustment of Antenna-1 has led to get its resonance around 28GHz; however, the operating bandwidth provided is only 1GHz, with the reflection coefficient below - 10 dB is taken as reference, which is insufficient for 5G applications and the impedance matching should be further improved. In general, the CMPA is most common owing to its attractive radiation features and easiness of fabrication and analysis; nevertheless, the low operating band consists its main issue. Thus, geometric modifications are needed to ameliorate the working band of Antenna-1. In this regard, the second phase shown in Fig. 2b is executed with the concern to extend the operating bandwidth where the conventional circular antenna is transformed to a circular monopole antenna named Antenna-2. As shown in Fig. 2b, a set of three primary modifications have been assigned to Antenna-1 to generate

Fig. 2 Step-by-step evolutionary design **a** Antenna-1. **b** Antenna-2. **c** Proposed antenna



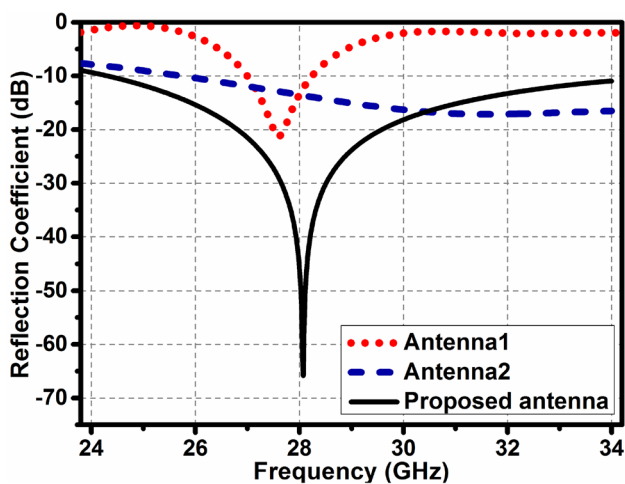


Fig. 3 Frequency response of the progressive designs

the large band characteristic. Firstly, the full ground plane is converted to a partial ground plane which is useful for the bandwidth extension; then, in the second step, a rectangular open-ended slot with dimensions of 1.52mm × 1.54mm is craved along the higher edge of the ground beneath the microstrip feeding line.

$$r1 = \frac{F}{\left\{ 1 + \frac{2h_s}{\pi\epsilon_r F} \left[\ln \left(\frac{\pi F}{2h_s} \right) + 1.7726 \right] \right\}^{1/2}} \tag{1}$$

$$F = \frac{8.791 \times 10^9}{f_r \sqrt{\epsilon_r}} \tag{2}$$

The truncated slot plays a crucial role to match the antenna input impedance across a long frequency range which results in wide operating band. Usually, the bandwidth enhancement can be achieved by employing a sizable ground plane compared to the radiating element [1]; however, in this design, the small etched slot serves to extend the bandwidth without enlarging the ground dimensions which contributes to preserve a small antenna dimensions. It is worth mentioning that the dimensions of the rectangular slot and the length of the partial ground plane have been attentively optimize through simulations to achieve the best antenna performance. In the third step, an extensive study have been performed on the feed-line width to well-suit the changes made on the antenna ground plane so Antenna-2 can finally fulfill the large band behavior as shown in Fig. 2. Nevertheless, the resonance at the desired frequency is lost which necessitates further changes to restore the resonating frequency. Therefore, the final phase is came with the aim to retrieval the antenna

resonant mode at the coveted frequency. Thus, in order to force the monopole antenna to manifest its fundamental resonance, it is requisite to upsurge the electrical current circulation on the radiating patch to more than that on the ground plane. For this reason, a circular cut is made inside the resonating patch which gives the final proposed design shown in Fig. 2c.

As anticipated, the reflection coefficient of the proposed antenna, presented in Fig. 3, shows that after etching the circular slot the antenna can finally recover the resonance frequency at 28 GHz with low reflection coefficient up to - 65 dB resulting in high impedance matching which is attained by a fine-optimization of the circular slot radius r2. The latter is fixed at 1.35 mm which is the eighth wavelength ($\frac{\lambda}{8}$) at 28 GHz. To gain better comprehension about the antenna behavior, Fig. 4 exposes the current distribution at the resonant frequency 28 GHz of Antenna-2 (without the circular slot) and the proposed antenna (with the circular slot). As demonstrated, for both designs, the ctric current flow tends to concentrate around the truncated slot in the ground, which indicates its primary role for ultra-wideband impedance matching. In addition, the insertion of the circular cut has led to a boost in the electrical current pervasion on the patch, where the slot has contributed to adding further edges (extra paths) for the current to pass through. So, by stretching the radius r2, the electric current trajectory is expanding, and the resonant frequency is progressively manifesting. Thus, the resonance at the desired frequency, i.e., 28 GHz, is finally reached. The reflection coefficient along with the input impedance of the proposed design is visualized in Fig. 5. As shown in Fig. 5a, the reflection coefficient of the proposed antenna is generated using the computational electromagnetic simulator CST. As revealed, the suggested design assures an ultra-wideband characteristic where the antenna is resonating at 28 GHz and covers a large bandwidth of 10 GHz from 24 to 34 GHz. The operating band combines several potential 5G bands such as 24.25–27.5 GHz, 26.50–29.50 GHz, 27.50–28.35 GHz, 29.1–29.25 GHz, and 31.4–33.8 GHz which can be used for several applications and in various geographical areas. The real part Re [Zin] and imaginary part Im [Zin] of the input impedance Zin of the antenna over the operating band is shown in Fig. 5b. In order to get an excellent impedance matching at a certain frequency, the resistance (real part) and the reactance (imaginary part) should be near to 50Ω and 0Ω, respectively, which is successfully satisfied by the proposed antenna at the operating frequency 28 GHz where the resistance is 49.95 Ω and the reactance is 0.002 Ω.

2.3 Parametrical study

In antenna designing, parametric analysis is an obligatory step to identify the optimum parameters values that will

Fig. 4 Surface current distribution at 28 GHz for **a** Antenna-2 (without circular slot). **b** proposed antenna (with circular slot)

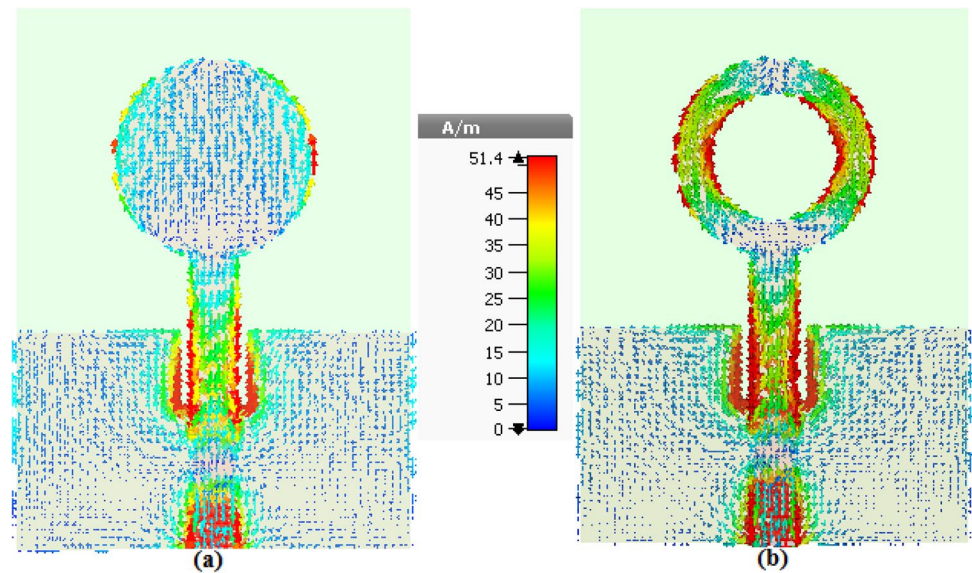
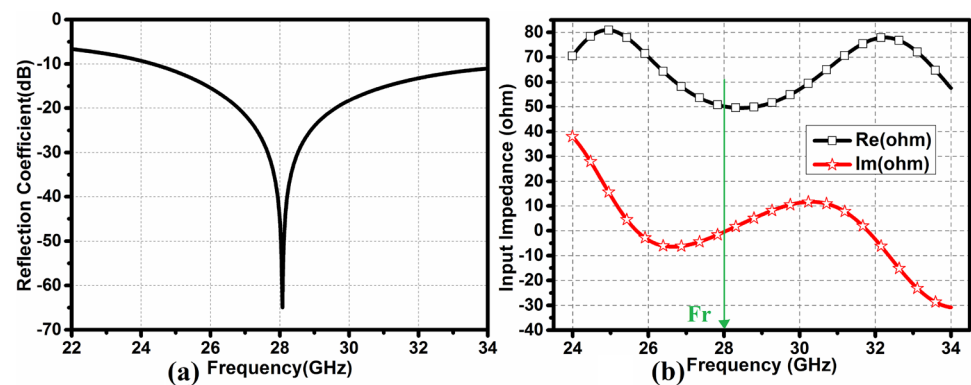


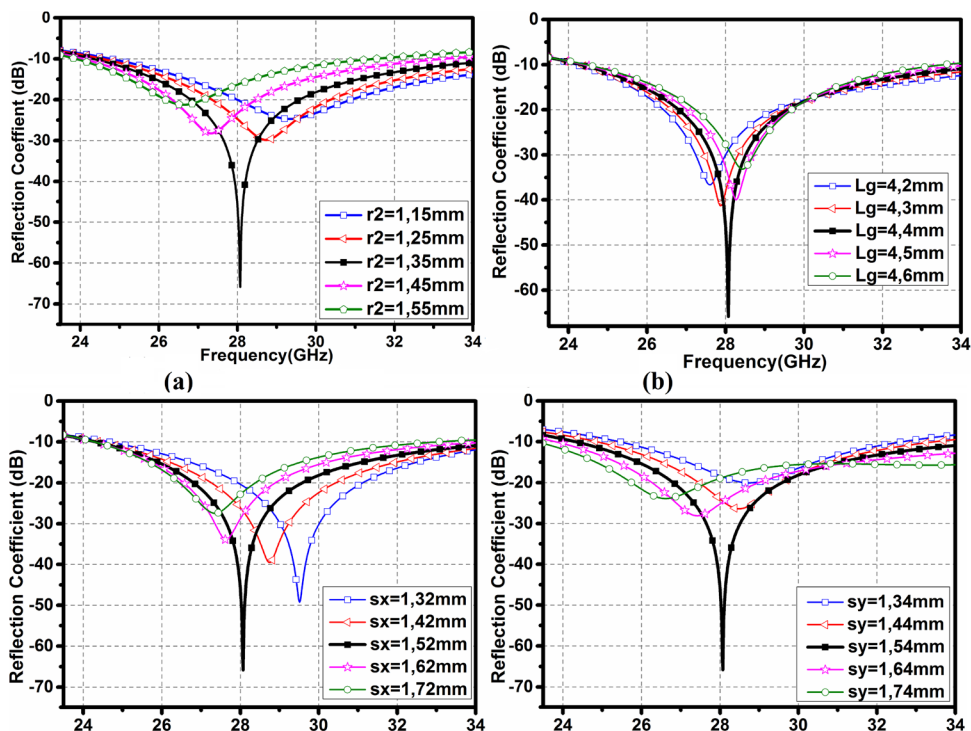
Fig. 5 **a** Simulated reflection coefficient extracted from CST software. **b** Real and imaginary part of the input impedance of the proposed antenna



allow the best antenna performance to be extracted. The objective behind this parametrical study is to demonstrate the impact of the parameters related to the circular cut, the ground plane and the open-ended slot on the adjustment of the antenna resonant frequency at 28GHz with the most improved impedance matching. The effect of the radius r_2 , the length of the ground plane L_g , and the dimensions of the rectangular slot s_x and s_y are manifested in Fig. 6. When a parameter is altered during the parametric analysis, the others remain fixed. As shown in Fig. 6a, when the radius r_2 of the circular slot is swapped from 1.15mm to 1.55mm with a step of 0.1mm, the operating frequency is gradually decreased from 29.2GHz to 26.5GHz, while, at the optimized radius $r_2=1.35$ mm, the resonance of the antenna coincides with the sought-after frequency with the optimized impedance matching. The influence of changing the length L_g of the ground plane is shown in Fig 6b. As observed, the effect of increasing the variable L_g from 4.2mm to 4.6mm has led to change the resonant frequency from 27.7GHz to 28.5GHz, where the desired resonance frequency is achieved at the optimal length $L_g = 4.4$ mm. Figure 6c depicts the

effect of the width s_x related to the open-ended slot on the reflection coefficient. As demonstrated, a noticeable effect is occurred on the resonating frequency when the width s_x is shifted from 1.32mm to 1.72mm, whereas the resonant frequency is moved from 29.5 GHz to 27.2 GHz, while the intended resonance at 28 GHz is reached with the lowest reflection coefficient of -66 dB when the width s_x gets the value of 1.52mm. The impact of the length s_y on the frequency response of the antenna is brought in Fig. 6d. As seen, in similar way, the variation of the rectangular slot length s_y from 1.34mm to 1.74mm affects significantly the resonant frequency and the impedance matching of the antenna where the resonating frequency is altered from 28.7 GHz to 26.5 GHz, and the optimal response is noted at $s_y=1.54$ mm. Therefore, the executed parametric study has shown that the variables including the circular slot radius denoted by r_2 , the length L_g of the ground plane, the width s_x and the length s_y of the rectangular cut in the ground plane play all an essential role in controlling the resonant frequency along with providing a proper impedance matching.

Fig. 6 Effect of varying some parameters on the reflection coefficient behavior **a** parameter r_2 . **b** parameter L_g . **c** parameter s_x . **d** parameter s_y

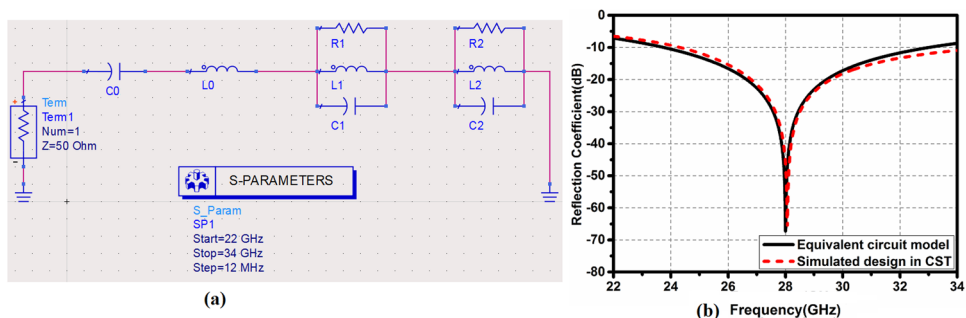


2.4 Equivalent circuit diagram

The equivalent electrical circuit diagram of the suggested UWB antenna is shown in Fig. 7 together with its corresponding frequency response. The circuit modeling step is performed with the assistance of the advanced design system environment software well-known by ADS simulator. One manner to carry out the electric circuit of an UWB antenna is to envisage it as a combination of multi-resonators mounted in series [26]. As shown in Fig. 7a, two resonating parallel RLC cells are linked in series to establish the antenna equivalent circuit model, where the resonant units number can be increased or decreased according to the desired resonances. For the proposed design, the equivalent circuit is performed based on the antenna input impedance shown in Fig. 5b, where the

number of the resonant cells is related to the number of the local maxima in the real part (resistance) of the input impedance at which the imaginary part (reactance) is near to 0Ω . As the antenna resistance (real part) has two local maxima, the electrical circuit is designed using two parallel RLC elements, while C_0 and L_0 denote the capacitance and the inductance of the antenna at the maxima with the lower frequency [27]. During the simulation process, the values of the lumped components are wisely fine-tuned to achieve the most matched frequency response with the envelope of the reflection coefficient and the resonant peak as well. Hence, the following, are the final optimal values of the lumped components: $L_0=6.77\text{pH}$, $C_0=11.57\text{pF}$, $R_1=49.98\Omega$, $C_1=0.23\text{pF}$, $L_1=140.12\text{pH}$, $R_2=32.14\Omega$, $C_2=10.02\text{pF}$, $L_2=100.1\text{nH}$, resulting in a very good coherence with the reflection coefficient extracted from CST software as shown in Fig. 7b.

Fig. 7 **a** Antenna equivalent circuit diagram. **b** comparison of the reflection coefficient response delivered by both CST and ADS



2.5 Measurement results and radiation features

As shown in Fig. 8a, in order to validate the simulated results, a manufactured prototype of the final optimized antenna is realized and tested. The antenna excitation is accomplished using the SMA connector, while the S-parameters measurement is done with the assistance of the Keysight (Agilent Technologies) E8363A 45MHz–40GHz (ENA series) Network Analyzer, as shown in Fig. 8b. A comparison of the measured and simulated reflection coefficient is carried out in Fig. 8c. As revealed, the fabricated prototype shows a high performance where the measured and simulated reflection coefficient are in good accordance with slight differences which can be attributed to the fabrication tolerances, SMA connector soldering, RF feeder cable,

and the testing environment. The measured reflection coefficient discloses an ultra-wideband functioning from 24 to 34 GHz with high impedance matching and a low reflection coefficient up to -40 dB at the measured resonant frequency around 28 GHz which confirms the proposed design validity.

Figure 9a presents a simplified diagram of the experimental setup used to measure the antenna radiation patterns within the anechoic chamber. As described, the radiation pattern testing is implemented using two antennas, the first one is the standard gain Horn antenna placed in the left extremity which is employed as transmitter antenna, while the second one placed in the right extremity is the suggested antenna defined as the antenna under test (AUT), playing the role of the receiver antenna mounted to a controllable rotating stand through a stepper motor controller, served for

Fig. 8 **a** Suggested antenna fabricated prototype. **b** measurement setup. **c** comparison of the measured and simulated reflection coefficient

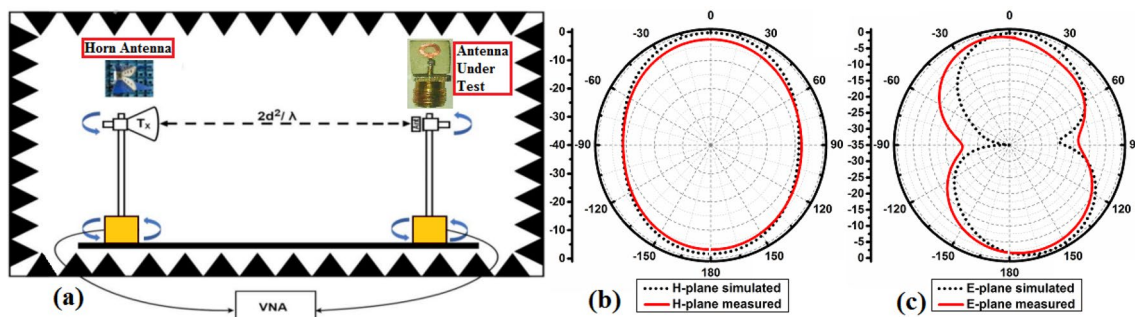
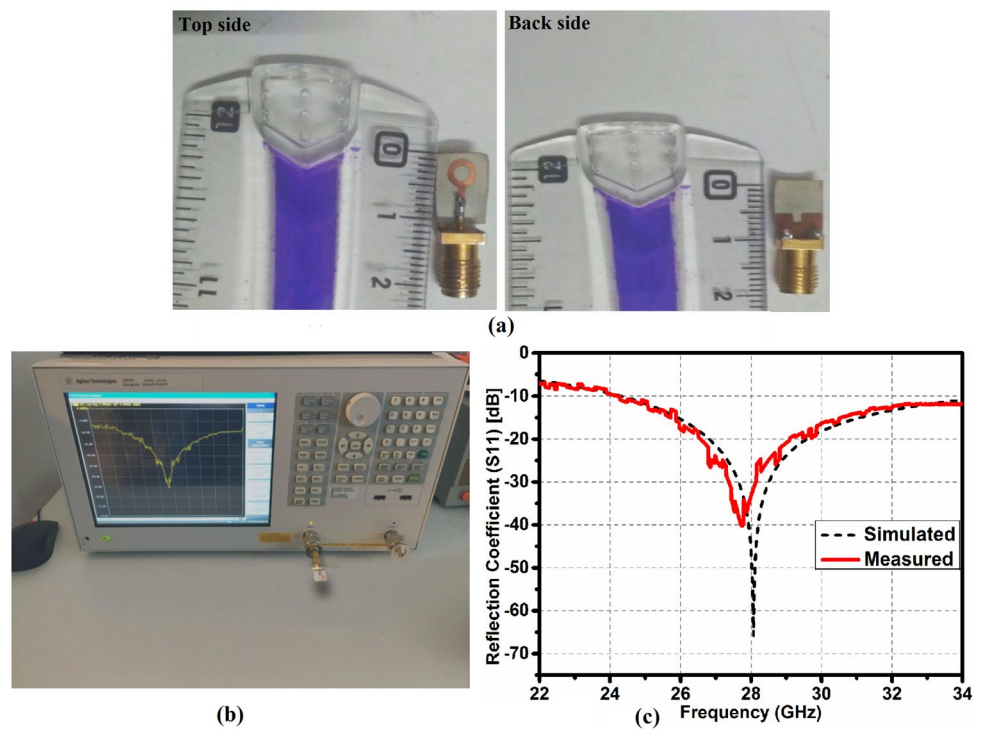


Fig. 9 **a** Streamlined schematic of the proposed antenna in the anechoic chamber. **b** measured normalized radiation pattern at 28 GHz in H-plane and **c** E-plane

the measurement process. The two antennas are situated in line of sight aligned to each other, where the Horn antenna is connected to the excitation source, and the AUT is linked to the other port of the vector network analyzer to measure the received power which is recorded using a driving software. The far-field normalized radiation pattern is measured at the resonant frequency of 28GHz in both principal H- and E-planes, where a comparison with the simulated radiation patterns is plotted in Fig. 9b, c respectively. As manifested, the simulated and measured patterns proved a high convergence level in both planes with good radiation trait, where the antenna possess a quasi-omnidirectional pattern in the H-plane (xoz) and a bidirectional pattern in the E-plane (yoz). In addition, as shown in Fig. 10a, the polar radiation pattern have been simulated at various frequencies including 24GHz, 26GHz, 30GHz and 32GHz. It is revealed that the suggested antenna maintains generally, a notably stable radiation pattern property throughout the ultra-wide operating band which is certainly desired for the good antenna performance. Furthermore, the gain and the radiation efficiency of the antenna along the entire bandwidth is configured in Fig. 10b. A high radiation capabilities are shown, where the radiation efficiency is greater than 98.7% in the whole band, while a reasonable gain no less than 4.8 dB is reached with a maximum value up to 5.9 dB.

3 Proposed MIMO antenna design and investigation

The employment of the MIMO systems is considered indispensable to implement the 5G infrastructure owing to its ability to significantly increase the channel capacity without wasting the bandwidth or the transmitting power. Nevertheless, some critical challenges are appearing while designing a MIMO antenna such as ensuring to keep a small size to suit the restricted space reserved for the antenna placement into the wireless devices in addition to provide a highly isolated MIMO elements by reducing the mutual coupling which badly affects the MIMO performance. Indeed, the mutual coupling defines the quantity of energy connected to an adjacent antenna when a MIMO antenna element is excited. It has a considerable effect on the MIMO diversity performance as well as the impedance and radiation characteristics, necessitating to be carefully reduced [28]. There is three principal categories to reduce the mutual coupling. The first category includes the decoupling scheme using spatial and polarization diversity. The spatial diversity is executed by significantly distancing the MIMO elements which is impractical and not convenient, while the polarization diversity is performed by vertically placing the elements which produces an orthogonally polarized MIMO antenna elements, leading to create uncorrelated channel resulting in low coupling effect. In general, polarization diversity is the most attractive method as the antenna elements can be closely positioned to each other while preserving a weak mutual coupling level. The second category

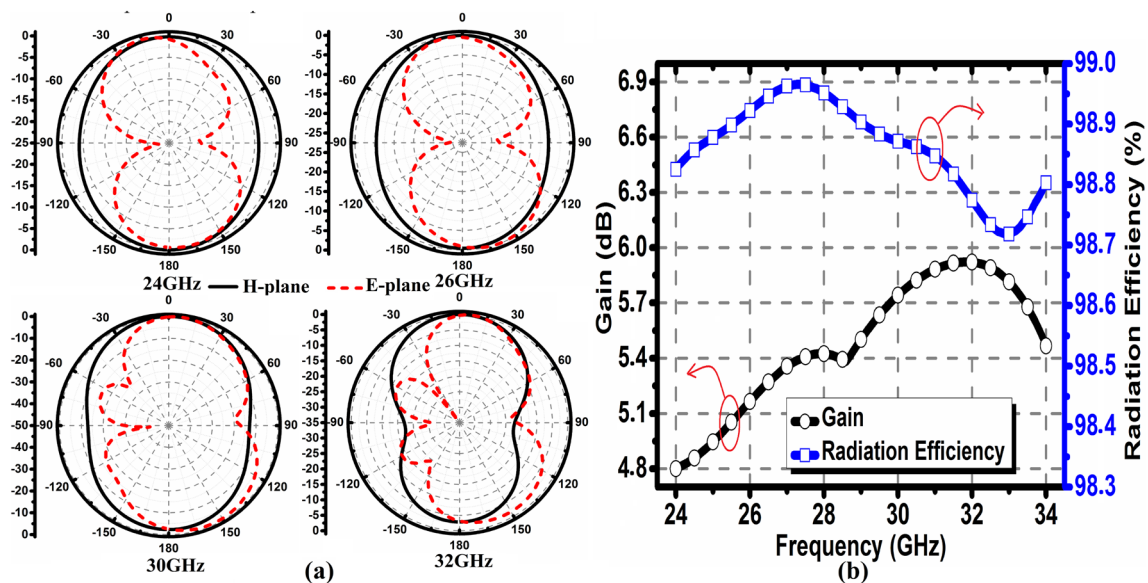


Fig. 10 a Simulated normalized radiation pattern at different frequencies within the operational band. b Radiation efficiency and gain versus frequency

involves inserting the decoupling structure such as parasitic structure, neutralization line, metamaterial, and defected ground structure (DGS) to block or suppress the coupling. The employment of such decoupling scheme may require additional space and bring a certain degree of complexity to the MIMO design if complexly created. However, if appropriately developed, it could be a good option when increasing the MIMO elements' number to concomitantly maintain compact size and satisfactory isolation. The third and final category is hybrid, and it combines the two previous categories. In this work, both polarization diversity and decoupling structure have been adopted to fulfill high isolation level while keeping a compact and simple layout.

3.1 Geometry of the proposed MIMO antenna and frequency response

Figure 11a exposes the configuration of the proposed 2 x 2 MIMO antenna, constructed based on the monopole antenna discussed above. As seen, the suggested MIMO system is established by vertically placing two units of single antenna on the same Rogers RT5880 laminate with a full area of 11 x 20.5 mm² and a spacing d of 2.5 mm, while the structure can be further developed by augmenting the elements number. As both elements provide linear polarization, the orthogonal arrangement would certainly be responsible to generate the polarization diversity, resulting in improved isolation.

The overall structure as well as the element spacing d have been wisely refined through the simulation to find the most balanced design that simultaneously combines between the sought-after results and the miniaturized dimensions. The fabricated model of the final MIMO antenna design is shown in Fig. 11b where two SMA connectors have been used to excite the structure. The corresponding simulated and measured S_Parameters are given in Fig. 11c, d, respectively. As clearly remarked, the measured and simulated S_Parameters agreed very well, where an ultra-wideband operation is assured by both elements with good impedance matching besides a high isolation exceeding 25 dB along the entire bandwidth.

With the intention to highlight the usefulness of the arrangement chosen in this study, the two-antenna elements have been differently positioned on the same substrate of the same size. As shown in Fig. 12, three different placements have been considered, the first one is the parallel structure (conventional) where the elements are placed in parallel, adjacent to each other. The second one (denoted by anti-parallel structure) puts the elements in opposite position. The third one presents the proposed arrangement where the elements are situated orthogonal to each other. It should be mentioned that for the three configurations, the two radiating elements were placed at a fixed distance d of 4.5 mm. The mutual coupling of the three configurations are demonstrated in the same Fig. 12. As manifested, the conventional

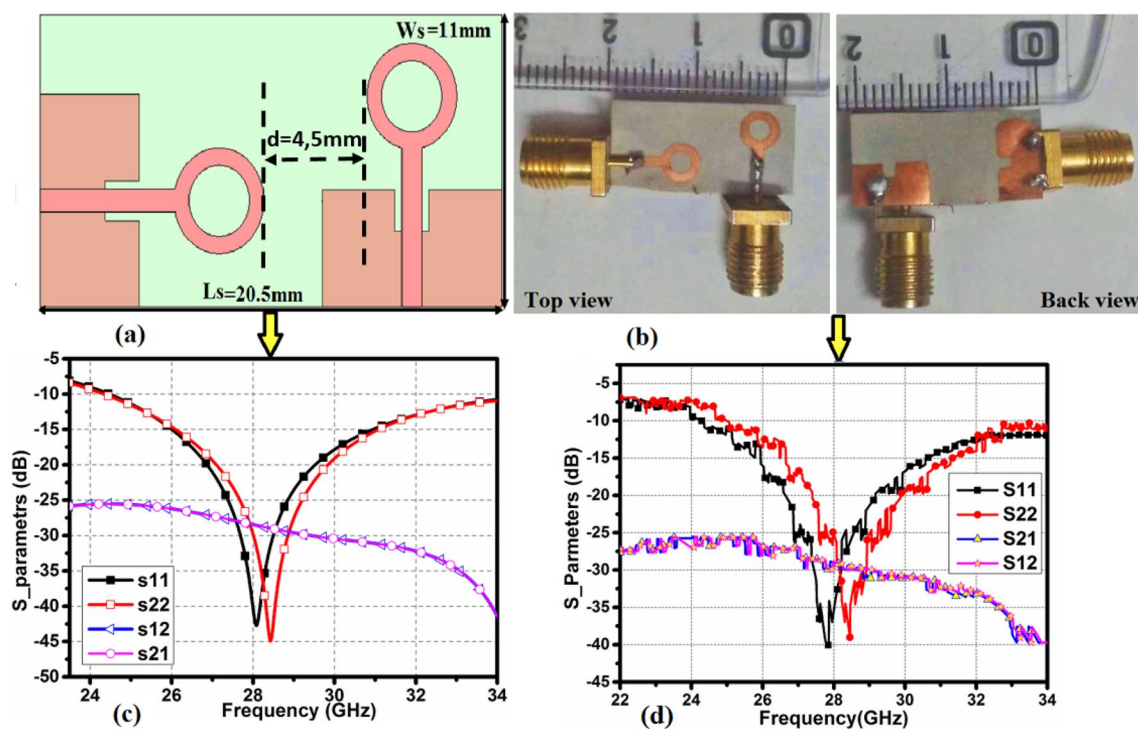
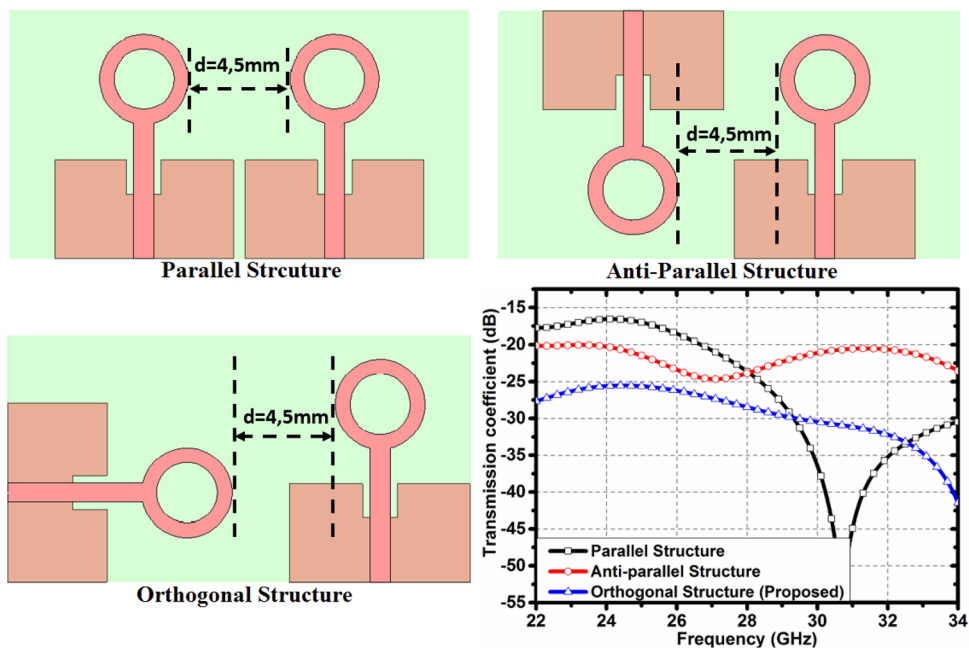


Fig. 11 a Geometrical layout of the proposed MIMO antenna. b fabricated model. c simulated S_Parameters. d measured S_Parameters

Fig. 12 Configuration of different MIMO arrangements accompanied with their related mutual coupling



parallel arrangement has led to achieve the lower isolation specifically in the lower edge of the operating band where the maximum mutual coupling is near to -16 dB which is expected as both elements have the same plane of polarization allowing high coupling energy to be induced between each other. For the second structure, where the antennas have an opposite direction, the mutual coupling is slightly reduced to less than -20 dB along the whole band. However, when the antenna elements are perpendicular to each other, the isolation is considerably enhanced to more than 25 dB in the entire bandwidth with an enhancement amount up to 9 dB as compared to the parallel structure. Indeed, the reduction in the mutual coupling is attributed to the orthogonal direction of the E-field vectors (cross-polarized orientation of the electric field vectors) generated by the perpendicularly placed antennas which results in non-overlapping E-field components. Therefore, the coupled energy between elements is inherently weakened, contributing to ameliorated isolation.

3.2 MIMO diversity performance

In order to legitimize the MIMO antenna performance, a set of some essential metrics have been carefully analyzed, which include the envelope correlation coefficient (ECC), the diversity gain (DG), the total active reflection coefficient (TARC), the channel capacity loss (CCL), and the channel capacity (CC). The ECC is deemed a preeminent parameter to be calculated to assess the MIMO competency. It defines the correlation level between the radiation patterns provided by the MIMO antenna elements linked in a single unit when they operate simultaneously. In the ideal case, the ECC

should be 0 which indicates a perfectly uncorrelated system. However, in accordance with the 3GPP specifications, for a highly uncorrelated system, the ECC should not exceed the practical industrial standard specified at 0.5 [29]. It can be determined by using the 3D radiation pattern expressed by Eq. (3) [30], which is valid for an isotropic wireless environment and considered the most accurate approach to determine the correlation for any lossy antenna.

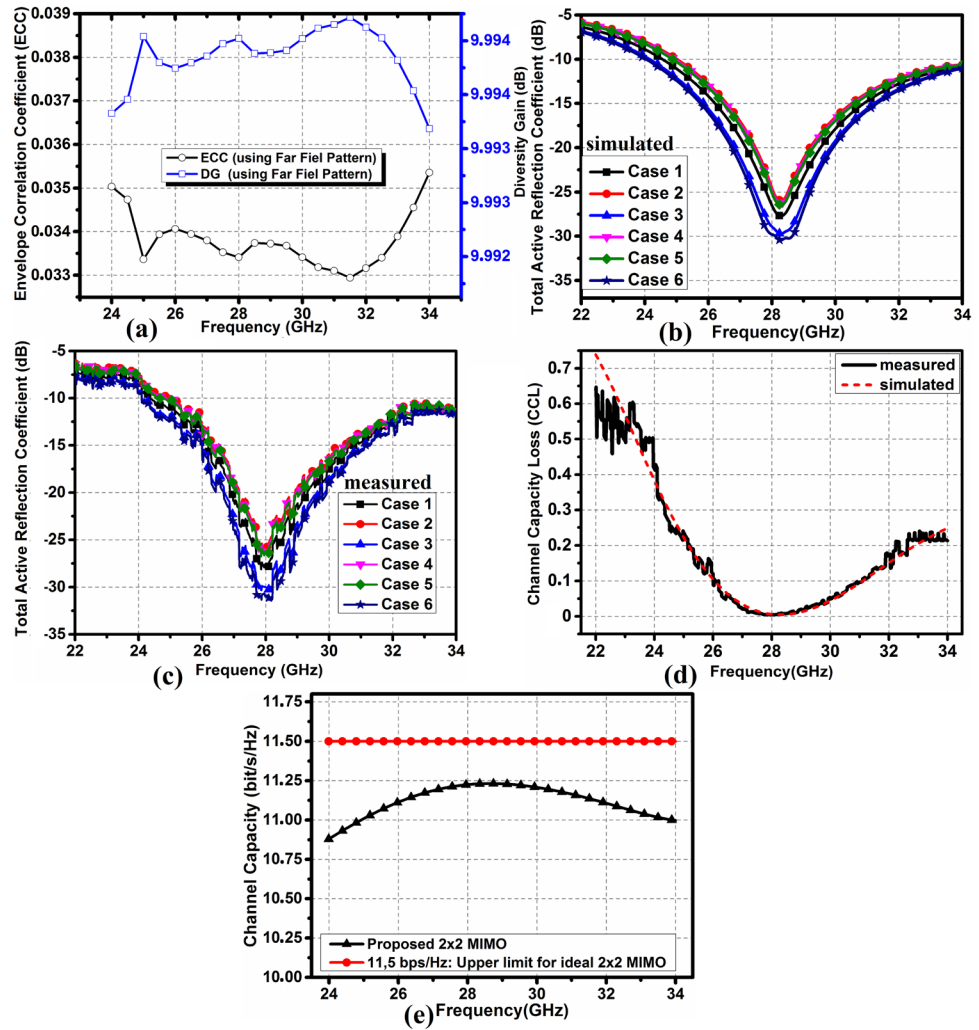
$$ECC_{ij\text{Far-field}} = \frac{\left| \iint_{4\pi} E_i(\theta, \varphi) \cdot E_j^*(\theta, \varphi) d\Omega \right|^2}{\iint_{4\pi} |E_i(\theta, \varphi)|^2 d\Omega \iint_{4\pi} |E_j(\theta, \varphi)|^2 d\Omega} \quad (3)$$

where $E_i(\theta, \varphi)$ and $E_j(\theta, \varphi)$ denote the complex 3D radiated electric field pattern of the i^{th} and j^{th} antennas, respectively, with $i, j = 1, 2$ for the proposed two-element MIMO antenna. The asterisk and the symbol “.” indicate the complex conjugate and the Hermitian product, respectively. The solid angle is denoted by Ω .

The computed ECC is shown in Fig. 13a. For easiness purpose, the ECC has been determined based on simulated far-field pattern. As the measurement using 3D radiation patterns involves a time-consuming integral computation. Hence, through the perusal in the obtained ECC parameter, a high performance can be observed, where the ECC is no more than 0.036 across the whole working band (24–34 GHz), which greatly respect the agreed threshold and prove a highly uncorrelated system.

Diversity gain (DG) is another paramount parameter to examine the MIMO diversity performance. The DG presents the enhancement amount in the SNR (signal-to-noise ratio)

Fig. 13 Diversity performance assessment **a** ECC and DG using radiated field. **b** simulated TARC. **c** measured TARC. **d** CCL. **e** CC



when a spatial diversity scenario is applied. In other word, it is the difference in decibel (dB) between the attenuation on a single link and a link with diversity channel in a fading environment. It can be calculated using Eq. (4) [31]. As expressed, the lower is the ECC, the higher is the DG. In the practical case, the DG should have a value close to 10 dB for high-level diversity performance. As shown in Fig. 13a, the mentioned criteria is excellently fulfilled by the proposed MIMO antenna, where the DG is more than 9.99 dB in the entire bandwidth.

$$DG = 10\sqrt{1 - ECC^2} \tag{4}$$

The next essential parameter to be verified is the total active reflection coefficient abridged by TARC. For an N-port MIMO antenna, this metric is determined by the square root of the total outgoing power (reflected power) from the all N-port divided by the total incident power to the all N-port [30]. It can be understood as the reflection coefficient of whole MIMO antenna where it can serve to

determine the effective bandwidth of the MIMO antenna system [29]. It is a real number varied between 0 and 1 where 0 signifies a total radiation of the incident power, while 1 signifies a total reflection of the incident power. For a two-port MIMO antenna, the TARC can be computed using Eq. (5) [30], where several parameters are involved such as the scattering parameters and the phase of excitation θ to consider the random summation effect of the signals at each port. The scattering parameters related to the first port are assigned with no excitation phase (e^{j0}), while the signals of the other ports are subjected to arbitrary excitation phase. Therefore, the simulated and measured TARC are calculated considering six combination cases of the excitation phase, where the latter is arbitrary chosen in the range 0–180°. The six considered cases are described as follows: case-1: 0°; 30°/case-2: 0°; 50°/case-3: 0°; 90°/case-4: 0°; 120°/case-5: 0°; 150°/case-6: 0°; 180°.

As shown in Fig. 13b and c, a good coherence is noted between both simulated and measured TARC for all treated cases. Indeed, despite the different excitation phases, it can

be clearly seen that the TARC metric has regenerated the curve envelope of the reflection coefficient provided by the single antenna with a value less than -10 dB along the entire working band, which proves the rigidity and the strength of the bandwidth provided. It seems convenient to mention that the TARC fastness is due to the low mutual coupling assured between the MIMO elements, while the slight differences are attributed to the various cases chosen where case-6 shows the most optimal result.

$$\Gamma_a^r = \sqrt{\frac{|S_{11} + S_{12}e^{j\theta}|^2 + |S_{21} + S_{22}e^{j\theta}|^2}{2}} \tag{5}$$

One other important metric to be analyzed is the channel capacity loss (CCL), it describes the uppermost accepted limit of the transmission loss, in bit/s/Hz, at which the high data transfer can be done reliably. Practically, to guarantee a high transmission rate, the maximum threshold accepted for the CCL is set at 0.4 bit/s/Hz [32, 33]. It can be easily determined using Eq. (6) where α^R denotes the receiving antenna correlation matrix. The computed CCL parameter from the simulated and measured scattering parameters is shown in Fig. 13d. As revealed, a very good agreement is proven by the simulation and measurement, where the CCL characteristic shows a desirable behavior below 0.4bit/s/Hz throughout the whole working band which provides a high reliable transmission rate.

$$C_{loss} = -\log_2 \det(\alpha^R) \tag{6}$$

where $\alpha^R = \begin{bmatrix} \alpha_{11} & \alpha_{12} \\ \alpha_{21} & \alpha_{22} \end{bmatrix}$, $\alpha_{ii} = 1 - (|S_{ii}|^2 + |S_{ij}|^2)$ and $\alpha_{ij} = -(S_{ii}^* S_{ij} + S_{ji}^* S_{ij})$ with $i, j = 1$ or 2

Furthermore, to deeply examine the performance of the suggested MIMO antenna design, the corresponding channel capacity has been calculated and compared with that of an ideal 2×2 MIMO antenna. The channel capacity (CC) defines the highest rate (upper bound limit) at which the information signal can be reliably transmitted through a given communication channel. In a simple term, the CC measures the number of bits that can transferred per one Hertz of bandwidth. It is employed to appear the capacity performance of the MIMO antenna relative to that of the single antenna, while it is also used to test the proposed MIMO performance in comparison with that of an ideal MIMO system. The CC calculation can be performed based on Eq. (7), where the identity matrix is denoted by I_{n_R} , the number of transmitting/receiving antennas are denoted by n_T/n_R , respectively. H_{scale} denotes the channel transfer matrix determined using Eq. (8), where $\rho_{scale,TX}/\rho_{scale,RX}$ is the transmitting/receiving correlation matrix, which consider the effect

of the total efficiency related to each MIMO element. H_{iid} is the channel matrix constructed based on the independent and identically distributed (i.i.d.) Rayleigh channel fading environment. The proposed MIMO antenna is taking the role of the receiving antenna, while the two transmitting antennas are considered ideal and perfectly uncorrelated (ECC = 0) with a total efficiency of 100%. It should be mentioned that the calculated channel capacity is performed by averaging a 10,000 realizations of the Rayleigh channel with a SNR of 20 dB. The CC of the proposed MIMO antenna is drawn and compared with that of the ideal case in Fig. 13e. As clearly remarked, the maximum channel capacity for an ideal two ports MIMO antenna is fixed at 11.5 bit/s/Hz, while the proposed design achieves a high channel capacity outstripping 10.87 bit/s/Hz along the whole operating band, which is attributable to the highly uncorrelated MIMO elements. In addition, a maximum amount of 11.25 bit/s/Hz has been reached around the resonant frequency, which approximately constitutes 97.8% of the ideal upper bound limit. As a result, the suggested MIMO antenna confirms its capability to fulfill a high channel capacity level in a fading environment with a maximum peak extremely close to the ideal case.

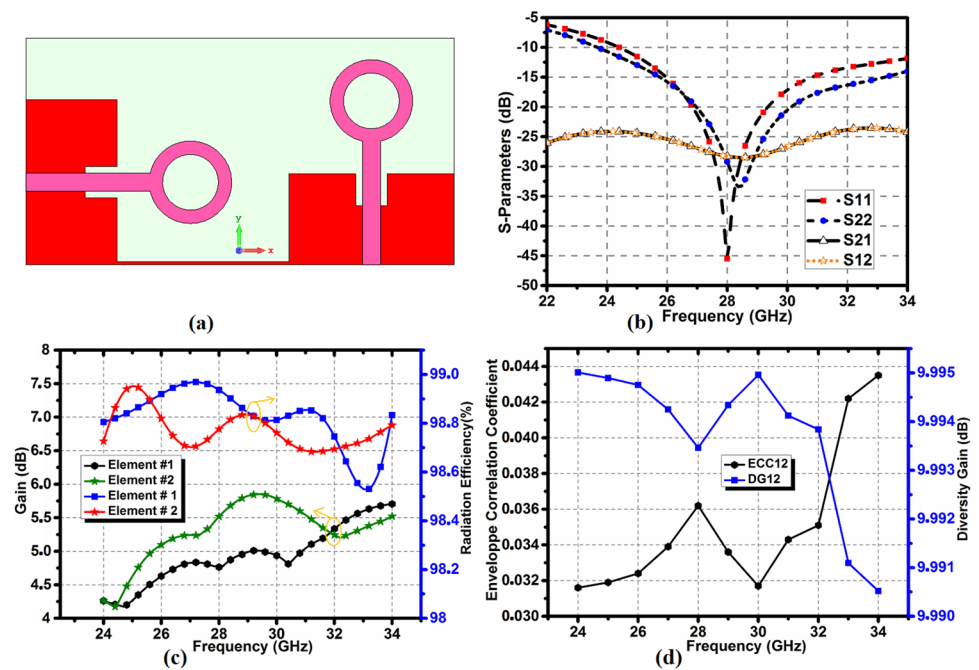
$$CC = E \left\{ \log_2 \det \left(I_{n_R} + \frac{SNR}{n_T} H_{scale} H_{scale}^T \right) \right\} \tag{7}$$

$$H_{scale} = \sqrt{\rho_{scale,RX}} H_{iid} \sqrt{\rho_{scale,TX}} \tag{8}$$

3.3 Connected ground plane effect

Considering the limited applicability of the MIMO antenna with separate ground planes, this subsection is dedicated to study the proposed MIMO antenna performance in the case of connected ground plane. Indeed, a common ground configuration is highly desired in the commercial field and much preferred to assure a smooth integration and ease operation of the wireless device where the MIMO antenna will be embedded. Accordingly, the layout of the MIMO antenna with connected ground is manifested in Fig. 14a. As displayed, the continuous ground structure is realized by linking the separate ground planes of elements using a simple 0.2-mm-width metallic strip. The strip-width is neatly selected after an intense parametric study to preserve a high MIMO antenna performance. The S-parameters of the obtained design is shown in Fig. 4b. As displayed, the connected ground structure does not significantly affect the MIMO antenna performance where both elements keep the UWB operation mode with good impedance matching in the band of interest, i.e., 24–34 GHz band, while the isolation has remarkably decreased to a minimum value of 23.6 dB, particularly in the higher frequency band which can be due to the electric current coupling among elements, engendered by the metallic interconnection. However,

Fig. 14 **a** Schematic of the proposed two-element MIMO antenna with connected ground plane. **b** Corresponding S-parameters. **c** gain and radiation efficiency vs frequency. **d** ECC and DG



although the employment of interconnected ground plane, the MIMO antenna still retains a high isolation exceeding 23.6 dB across the whole working band which is well-below the safe threshold determined at 15 dB [39].

The elements' gain and radiation efficiency across the operating band are drawn in Fig. 14c. As depicted, both MIMO elements achieve a reasonable gain and high radiation efficiency ranged between 4.2–5.9 and 98.6–99%, respectively, which show a decent radiation traits.

To better analyze the competency of the MIMO structure with continuous ground plane, the diversity performance has been addressed in terms of the crucial metrics, namely DG and ECC, where the latter is calculated based on 3D far-field patterns by Eq. (3) for an accurate result. Hence, the plot presented in Fig. 14d reports a desirable behavior where the ECC is remained below 0.044, and the DG is more than 9.99 along the entire working band which greatly respect the practical limits. Consequently, the achieved outcomes prove a good performance which ensure the validity and the applicability of the proposed design when used with connected ground structure.

4 Extended MIMO antenna array

To well-satisfy the 5G requirements, extending the MIMO elements' number in a system is much preferable, which will help considerably to upgrade the reliability and channel capacity simultaneously. On this basis, the main aim of this section is to carefully investigate the MIMO antenna competency and validity when the elements' number is extended

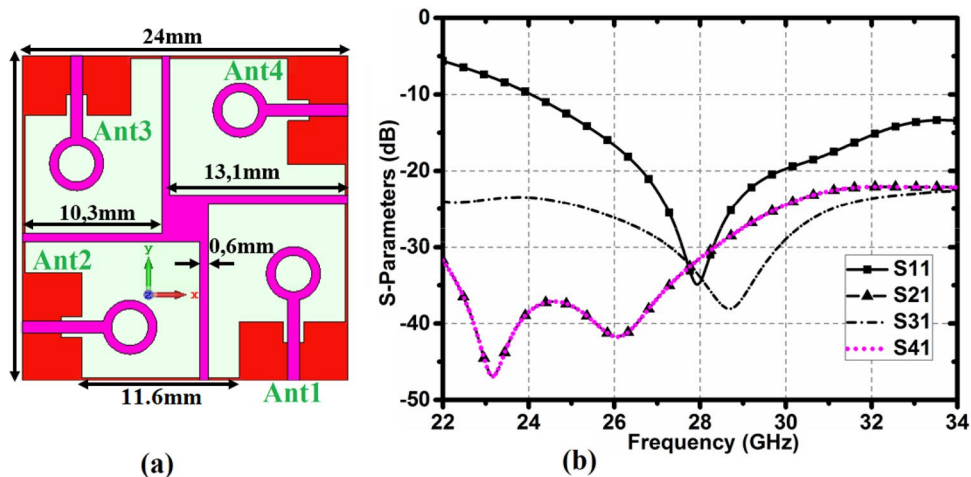
to four/eight-element. Along the performed study, the proposed MIMO systems have been neatly evaluated in terms of S-parameters, gain, radiation efficiency, ECC, and DG.

4.1 Four-element MIMO antenna

4.1.1 Layout configuration and derived S-parameters

Figure 15 depicts the complete structure of the proposed 4×4 MIMO antenna accompanied with its corresponding S-parameters. The four elements are referenced as Ant1, Ant2, Ant3, and Ant4. As observed in Fig 15a, the suggested layout can be easily obtained by replicating, shifting, and rotating the single-antenna unit studied above. The four elements have been arranged orthogonally on the same Rogers RT5880 substrate with a small footprint of $24 \times 24 \text{ mm}^2$, while the split ground planes have been unified using four metal strips with dimensions of $11.6 \times 0.2 \text{ mm}^2$ to meet the common ground plane necessity required in a real system. As aforementioned, the orthogonal disposition has been chosen as it engenders polarization diversity serving to weak the mutual coupling between perpendicular elements. Moreover, a fan-like isolating structure has been carefully constructed, optimized, and centered between the radiating elements on the top-side of the substrate to further improve the isolation among the elements provide spatial diversity, i.e., non-orthogonal elements (1,3) and (2,4) without extending the overall area. As seen, the fan-like decoupler consists of a square-shaped conductive patch placed in the middle with four metal strips attached to its corners, where all related sizes

Fig. 15 **a** Geometrical layout of the proposed 4 × 4 MIMO antenna. **b** Resulting S-parameters



are displayed with the configuration. During simulations, when an element is excited, the other ones are connected to 50-ohm matched loads. However, considering the symmetrical arrangement and similarity of elements, only the S-parameters pertaining to Ant1 are plotted in Fig. 15b to describe the achieved results. As shown, the proposed MIMO antenna preserves its resonant mode at 28 GHz with an UWB operation from 24GHz to 34GHz, besides assuring a high isolation where the worst-case isolation is more than 22.5 dB.

4.2 MIMO antenna evolution process

In order to well-know the effect of inserting the fan-like isolator, Fig. 16 displays the step-wise geometries followed to obtain the final design providing an optimized decoupling among the four exciting ports, where each step is presented with its respective S-parameters. As manifested in Fig. 16a, in the initial stage retained as reference, the design evolution mechanism is started with no decoupling structure where the elements are orthogonally disposed. As plotted, the respective scattering parameters (S-parameters) shows a good reflection coefficient characteristic with high impedance matching. Moreover, a low mutual coupling is achieved

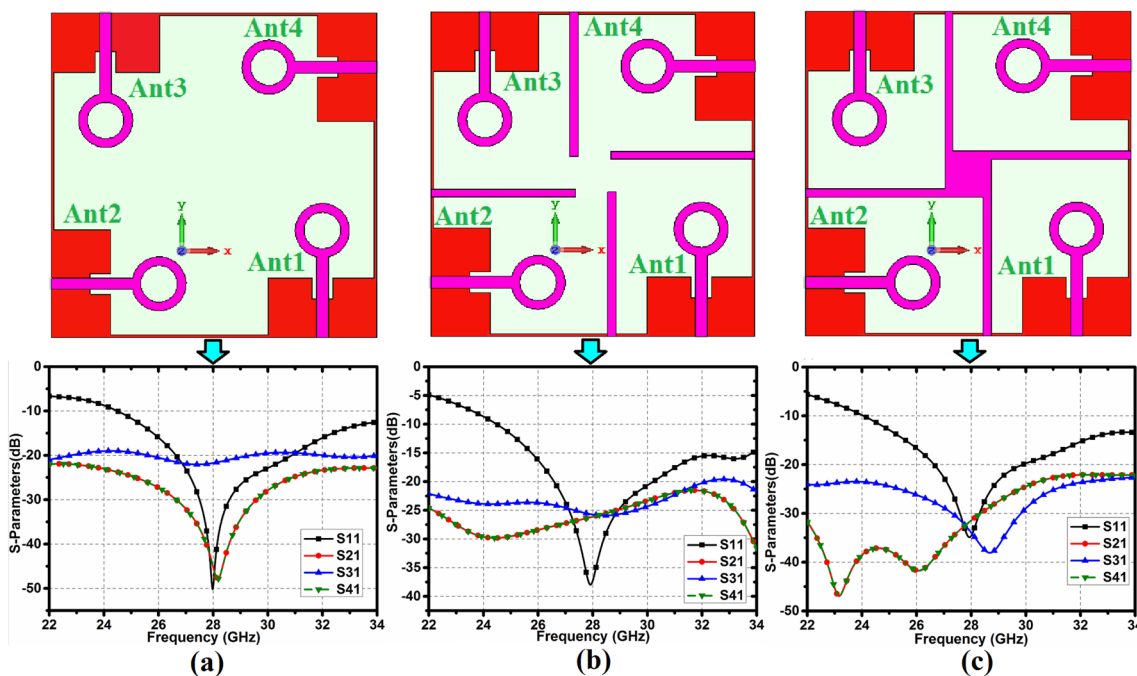


Fig. 16 Progressive steps of the MIMO antenna with decoupling scheme and associated S-parameters **a** stage-1. **b** stage-2. **c** stage-3

between the perpendicularly placed elements (S21 and S41) where the maximum coupling is lower than -22dB and the minimum coupling reaches to -49dB . However, the mutual coupling among diagonal elements (S31) is almost constant with a slight variation around -20 dB along the entire bandwidth which can be further minimized by using a simple decoupling mechanism. Hence, the next steps are executed with the intention to optimize the isolation between non-orthogonal elements. In the second stage, the decoupling mechanism is proceeded by including four conventional metal stubs between each two successive elements on the upper side of the substrate where the stubs' length (i.e., 10.9mm) is near to wavelength at 28GHz . The inserted stubs act as reflectors and serve to decrease the electromagnetic energy coupled to the diagonal units. As displayed, the related S-parameters response shows a 5 dB reduction in the mutual coupling between the diagonal elements where the minimum coupling achieved reaches a minimum value of -25 dB while the maximum value still fixed at -20 dB . In the third stage, another geometrical modification is performed to further boost the decoupling ability. As manifested in Fig. 16c, the last step is accomplished by combining the four isolating strips in the center of the substrate using a square-shaped patch which produces the final fan-like isolating scheme. As reported, the resulting structure is well-succeeded to improve the isolation performance. Indeed, the derived S-parameters shows an optimized outcomes especially in terms of the mutual coupling among diagonal element S31, where the latter is lower than -22.5 dB across the entire band and gets a minimum value up to -38 dB

around the resonant frequency. Furthermore, the reflection coefficient remains better than -10 dB over the $24\text{--}34\text{ GHz}$ band and assures a good impedance matching at the resonating frequency, while the orthogonal elements preserves a high isolation level ranging $22\text{--}42\text{ dB}$ along the operating band. Accordingly, it can be confirmed that the suggested fan-like decoupler has convincingly contributed to promote the isolation of elements without compromising the design simplicity or enlarging the overall area or affecting the bandwidth and the resonating frequency. Further evaluation of the MIMO performance regarding the radiation traits and diversity performance is taken place in the next subsection.

4.2.1 Radiation characteristics and diversity performance

Figure 17 illustrates the 2D far-field radiation patterns of the suggested MIMO antenna emitted from the orthogonal elements denoted by Ant1 and Ant2 in the two cut planes XZ ($\varphi = 0^\circ$) and YZ ($\varphi = 90^\circ$) at different frequencies along the operating bandwidth. As reported, the antenna elements provide a uniform radiation characteristic not distorted by the MIMO arrangement where the plotted far-field patterns are marked by a stable, focused, and directional radiation behavior at all selected frequencies, where the resulting radiation is most often oriented toward broadside direction (around 0°), which is desirable to assure reliable transmission at mm-wave spectrum. In addition, it is observed that the radiation patterns of Ant1 and Ant2 in XZ and YZ planes are totally reversed. More specifically, the E-plane (YZ) and H-plane (XZ) of Ant1 are found in opposite order for Ant2 which

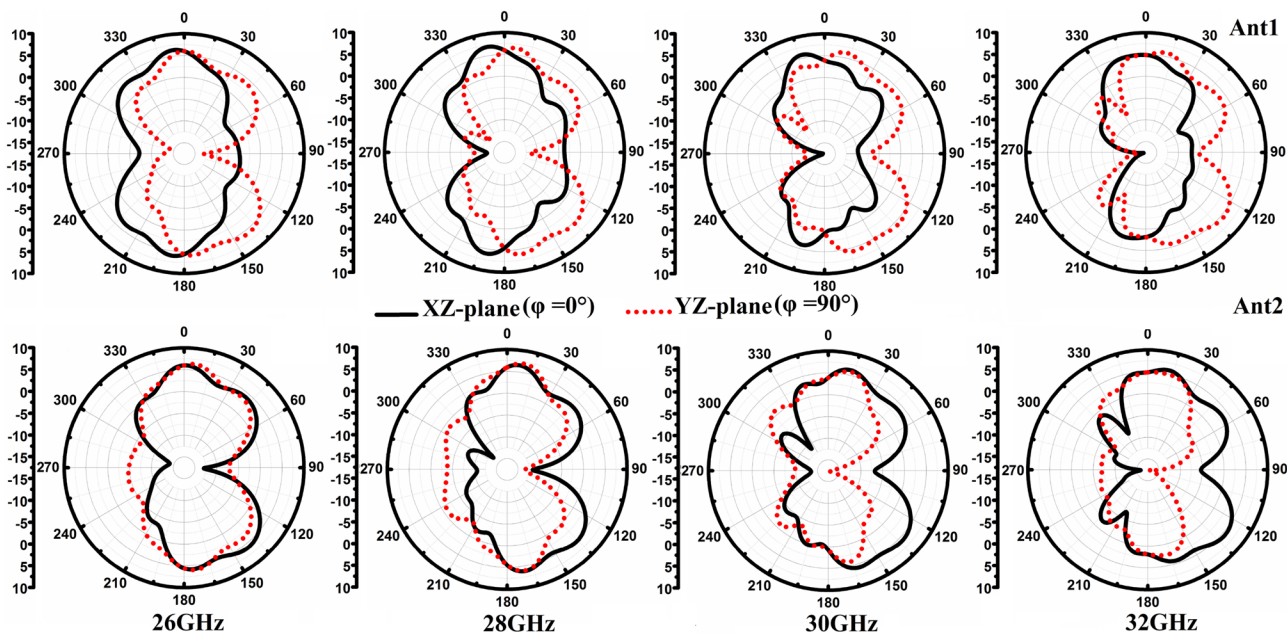


Fig. 17 Polar radiation pattern at various selected frequencies in the two principal XZ and YZ cutting planes

confirm the existence of polarization diversity phenomenon. This in turn could be potentially benefit to achieve uncorrelated far-field patterns, desired to reduce the multipath fading happened in a communication system. Next, in order to check the other radiation competencies, Fig. 18a depicts the gain and radiation efficiency of the MIMO antenna over the operational bandwidth. As seen, along the entire band, the proposed MIMO system is featured by a high radiation efficiency outstripping 98.2% and enhanced gain ranging 6.5–7.62 dB. Besides, the MIMO diversity performance has been evaluated in terms of some essential metrics such the ECC and DG determined using 3D far-field patterns. As reported in Fig. 18b, for orthogonal elements, the ECC is no longer than 0.04, and the DG is more than 9.99 dB, while in the case of diagonal elements, the ECC does not exceed 0.09, and the DG is above 9.96 dB across the operating ultra-wideband range which largely respect the agreed criteria. Thus, the attained outcomes emphasize the legitimacy of the proposed design and its appropriateness for employment as it combines between the small-dimension trait and the good operation behavior while using a quite simple decoupling structure.

4.3 Eight-element MIMO antenna

4.3.1 Proposed configuration and related S-parameters

This subsection is dedicated to carefully analyze the suggested eight-port extended MIMO antenna and validate its practicality. Hence, Fig. 19a depicts the geometrical design of the MIMO antenna built using the same aforementioned substrate. As manifesting, the radiating elements are positioned parallel, orthogonal, and opposite to each other within a full small-area of $39 \times 44.2\text{mm}^2$ where the elements' ground planes have been connected using 0.2-mm-thick metal strips with different lengths of 10.1mm and 11.1mm for parallel and orthogonal elements, respectively. Additionally, a wholly simple I-shaped decoupling structure is inserted among elements to improve the isolation and keep minimized dimensions where the related dimensions are displayed with the MIMO design. It is worth citing

that the final isolation structure is reached through a careful parametric study to find the optimum dimensions allowing the best isolation achievement. The concerned reflection coefficients are outlined in Fig. 19a where all elements show an ultra-wideband response from 24 to 34 GHz by reference to -10 dB with good impedance matching at the resonant frequency, i.e., 28 GHz. Moreover, Fig. 19b plots the transmission coefficients related to Ant1, while Fig. 19c presents the transmission coefficients between other selected antennas. As demonstrated, a high isolation performance is reported between all pairs of antennas where the minimum isolation achieved is more than 21 dB. Moreover, it is found that the majority of pairs have an isolation outstrips 25 dB in the most parts of the operating bandwidth, which can be considered a good compromise combining the high isolation level and the small size requirement for an eight-port MIMO antenna.

4.3.2 MIMO antenna evolution procedure

In order to highlight the effect of the decoupling structure, Fig. 20 displays the evolutionary stages of the MIMO antenna design together with their respective isolation responses. Given the elements' symmetrical arrangement and the similarity of the opposite elements' S parameters, only element pairs with non-similar mutual coupling responses have been shown, to avoid the congestion and repetition of curves. As shown in Fig. 20a, initially, the MIMO antenna design construction is proceeded without including any decoupling scheme where the eight-element are distributed along the substrate borders, while the ground planes are connected in the back side of the substrate. Through the perusal in the corresponding S-parameters, it can be remarked that all element pairs are featured by high isolation exceeds 20 dB across the whole spectrum range, except the isolation of elements placed in the middle of the substrate edges, i.e., the pairs (1, 4), (1, 6), (8, 4), and (8, 6) presented by S41 (as they all provide similar coupling effect), which reveals a relatively low isolation up to 17 dB toward higher frequency band. Accordingly, the next modification step is

Fig. 18 a Gain and radiation efficiency versus frequency. b computed ECC and DG based on far-field pattern

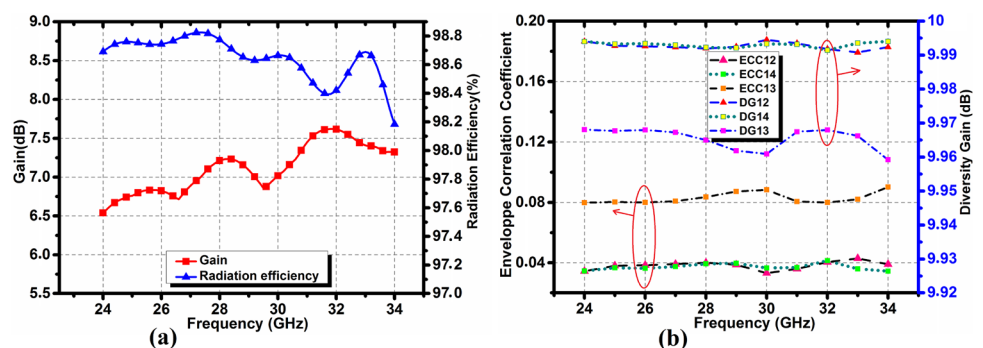
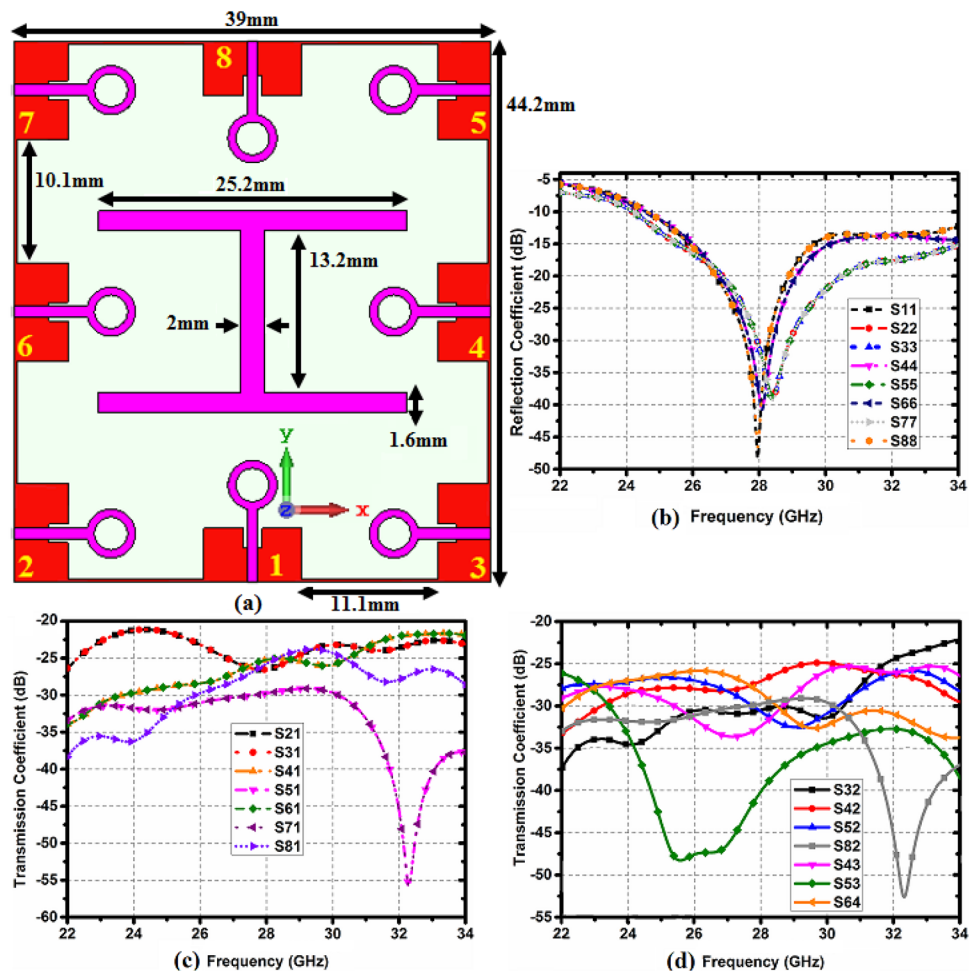


Fig. 19 **a** 8×8 proposed MIMO antenna. **b** reflection coefficient. **c** mutual coupling between Ant1 and other elements. **d** mutual coupling between other selected antennas



performed to further enhance the isolation of the mentioned elements.

For this aim, as shown in Fig. 20b, in the second stage, two metallic strips of size $1.6 \times 25.2\text{mm}^2$ are horizontally printed between the concerned elements to absorb the coupling energy and block its propagation from the excited antenna to the other elements. As expected, the resulting S-parameters prove the effectiveness of the inserted metal strips to improve the decreased isolation, detected in S41-parameter, from 17 to more than 21 dB in the whole band. In contrary, a significant dip is discovered in the isolation among the fourth and sixth elements (S46) after using the two horizontal strips which requires additional modification to handle this undesirable effect. Consequently, in the last stage reported in Fig. 20c, an extra metal strip of 2-mm-width and 13.2-mm-length is vertically embedded between the respective elements where it is connected to the two other isolating strips leading to attain the proposed I-shaped decoupling structure. The obtained S-parameters disclose a considerable improvement in the isolation between the fourth and sixth antenna element, where the added strip contributed effectively to capture the coupling

fields among the two elements which served to convincingly optimize the isolation to more than 25 dB in the whole band, while exceeding 30 dB at the higher frequency range. Therefore, the decoupling structure demonstrates its capability to guarantee convincing isolation between all the MIMO elements along with small size dimensions without yielding any design complexity.

4.3.3 Far-field radiations and diversity performance

Considering the similar performance delivered by symmetrical elements and opposite elements, there is no need to plot the radiation performance of all MIMO elements. Hence, Fig. 21 exhibits the polar far-field pattern (gain) in E-plane (YZ) and H-plane (XZ) for the elements Ant1, Ant2, and Ant4 of the proposed eight-port MIMO antenna at various selected frequencies, i.e., 26/28/30/32 GHz, where when an element is powered, the other ones are ended with 50 Ω matched loads. As revealed, the radiation behavior tends to be directive in both cutting planes at all selected frequencies for the majority of elements which is recommended for 5G communication. In addition, it is noted that various radiation

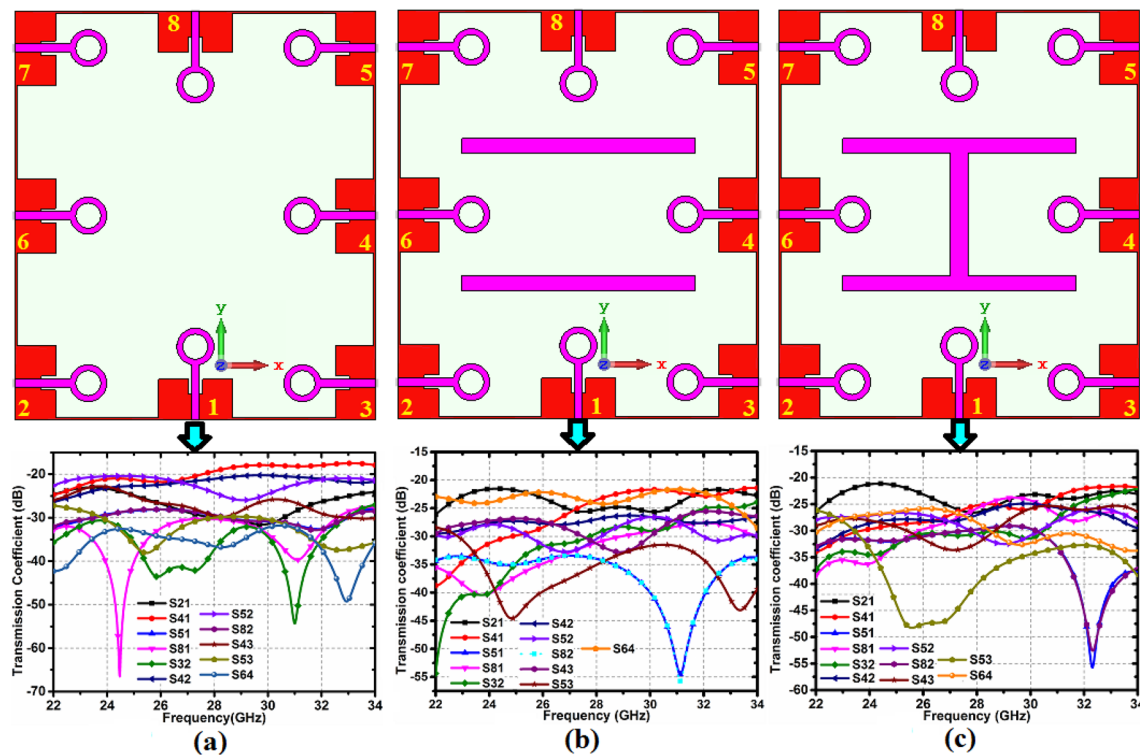


Fig. 20 Development stages of the 8-port MIMO antenna accompanied by the resulting isolation response **a** stage-1. **b** stage-2. **c** stage-3

patterns in different directions are acquired by the elements at the same frequency which could be helpful to provide pattern diversity.

The gain and radiation efficiency over frequency of Ant1, Ant2 and Ant4 is plotted in Fig. 22a. As shown, the three elements are marked by good gain trait ranging 5.3–7.8 dB, 6.5–8.5 dB and 6.9–8.3 dB, respectively, while a high radiation efficiency exceeding 98% is offered by all elements across the operational band. Furthermore, to legitimize the proposed MIMO antenna design and to well-examine its competencies, the diversity performance has been also analyzed in terms of ECC and DG based on radiation pattern method. As manifested in Fig. 22b, the ECC metric is less than 0.065 between all orthogonal pairs such as (1, 2)/(1, 3)/(1, 4)/(1, 5)/(1, 6)/(1, 7), while it does not exceed 0.14 between parallel pairs (3, 4)/(3, 5) and opposite element pairs (1, 8)/(2, 3)/(2, 4)/(2, 5)/(4, 6). The attained ECC is well-below the maximum permissible limit, i.e., 0.5, which indicates a low correlated elements, required for good transmission quality. In addition, the DG parameter is higher than 9.91 dB between all element pairs and reaches a maximum value up to 9.99 dB between orthogonal pairs, which shows a good MIMO diversity performance. Consequently, the achievements of the suggested 8x8 MIMO antenna prove its suitability for incorporation in 5G systems. This is attributed to several sought-after traits including the miniaturized dimensions while providing a good operation behavior.

5 Comparative study with the other existing works

In order to accentuate the performed work achievements, Table 2 brings a detailed comparison of the suggested 2 × 2 MIMO antenna design with the different state of the art including the MIMO and single antennas. Certainly, there is a plenty of research that have been reported in the literature as candidates for the 5G wireless systems which present various antenna designs operating in the ka-band (26–40 GHz) especially around 28 GHz band. Nevertheless, by reviewing the comparative table, it can be obviously seen that the suggested design outperforms the other MIMO systems by possessing the smallest physical dimensions especially comparing with those with the same number of elements. Additionally, despite its small size, the proposed MIMO antenna is distinguished by a highly isolated elements with an isolation outpaced 25 dB which strongly competes the other works with larger size. In the other side, the robust isolation served to provide a stellar diversity performance where all the examined metrics have greatly respected the practical limits, while the majority of the mentioned works are not investigated in terms of the TARC, CCL and CC, and some others had not addressed the MIMO structure. Moreover, the MIMO elements are featured by the highest radiation efficiency, a broad operating bandwidth, and a comparable reasonable gain without reference to any gain upgrading

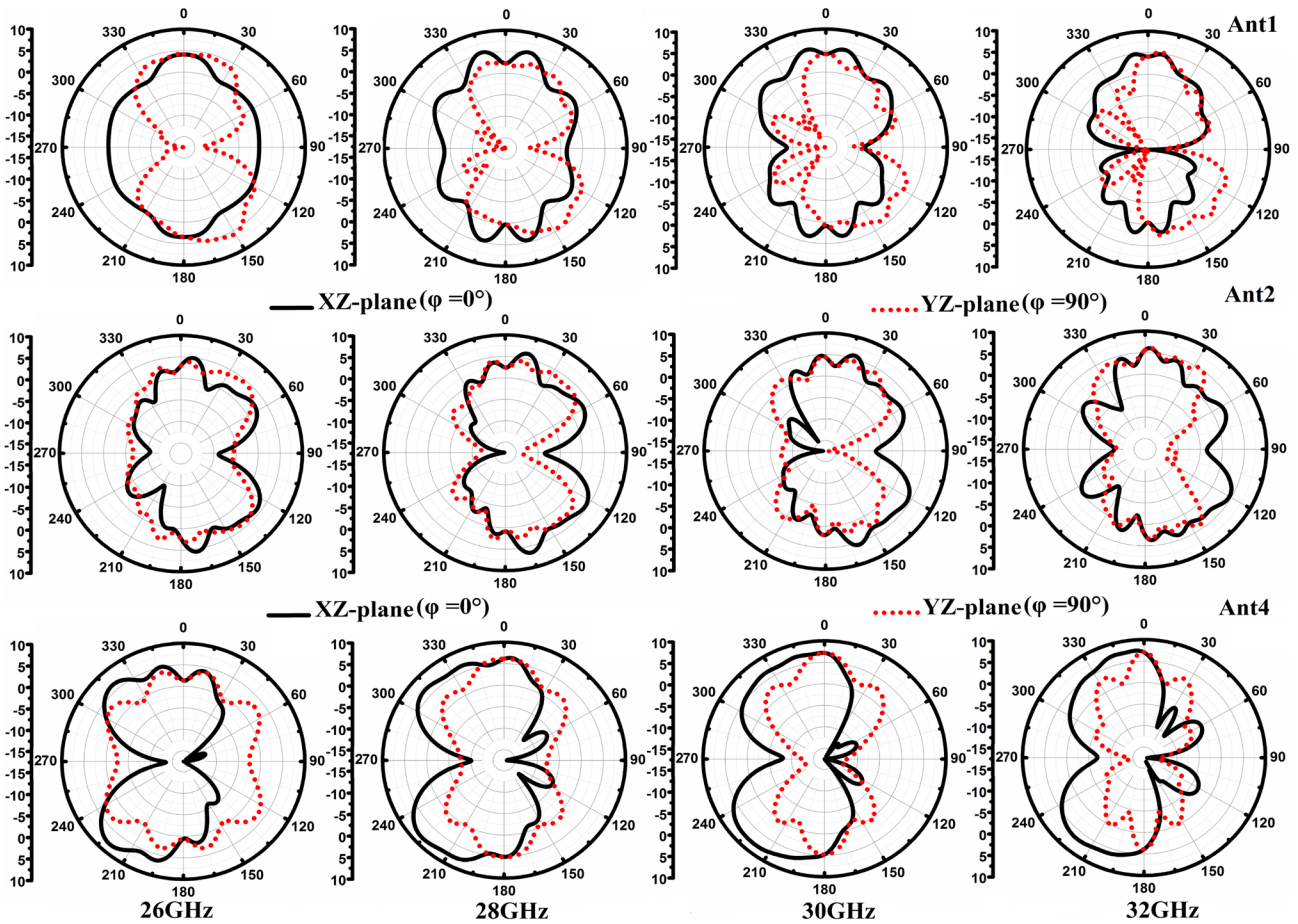
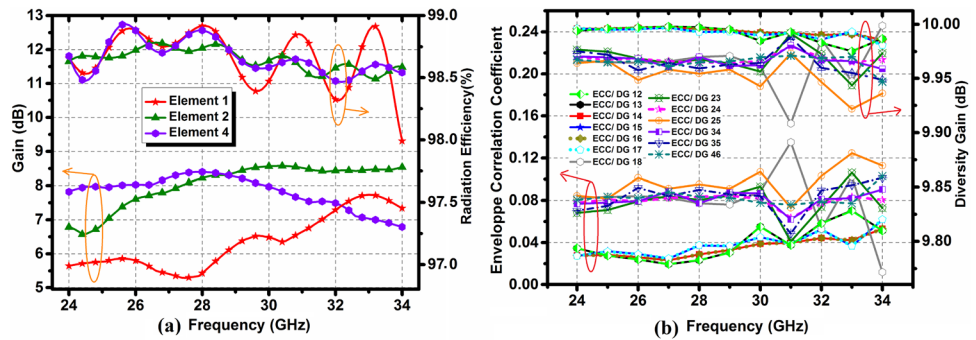


Fig. 21 Two-dimensional radiation pattern of the proposed 8-port MIMO antenna in XZ and YZ principal planes at various frequencies

Fig. 22 a Gain and radiation efficiency vs frequency, b computed ECC and DG using radiation pattern approach



mechanism while keeping a miniaturized and simple geometry. Similarly, the achievements of the proposed $4 \times 4/8 \times 8$ MIMO antennas have been also presented in the comparative table. As compared with the previous works, it can be noted that both structures preserve a small footprint with

high isolation, enhanced gain, high radiation efficiency, and sufficiently good diversity performance. Accordingly, it can be concluded that the proposed MIMO system combines a set of the most desirable traits which well-positioned it to be suitable for the 5G wireless systems.

Table 2 Results evaluation in comparison with the recently reported research

Ref	Size (mm ³)	No. of elemt	Fre-quency range (GHz)	Operat. BW (GHz)	Max. gain (dB)/efficiency (%)	Isolation (dB)	ECC/DG	CCL/CC (bit/s/Hz)/TARC (dB)	Substrate Material
[1]	26×11mm ²	2	25–29	4	5.7/> 97	> 20	<0.001/> 9.99	NA	Rogers 4003C
[7]	80×80×1.57	4	23–40	17	12/> 85	> 20	<0.012/ NA	NA	Rogers RT5880
[9]	50.8×12×0.8	4	25.1–37.5	12.4	10.6/> 80	> 20	<0.1/ NA	NA	Rogers RT5880
[10]	9.88×20.4×0.91	1	28 GHz-band	0.5	6.3/ NA	NA	NA	NA	Ceramic
[16]	12×14×0.38	1	27.7–28.2	0.5	8.2/> 94	NA	NA	NA	Rogers RT5880
[17]	14×26×0.38	2	26.65–29.2	2.55	1.83/> 76	> 20	<0.001/> 9.99	<0.4/ NA/ NA	Rogers RT5880
[19]	7×7×1.28	1	28.08–28.712	0.634	5.51/81 (at 28 GHz)	NA	NA	NA	Rogers RO3010
[20]	30×35×0.76	4	25.5–29.6	4.1	8.3/> 79	> 17	<0.01/ > 9.96	<0.4/ NA/ NA	Rogers R04350B
[22]	55×110×0.5	4	27.58–28.649	1.06	8.2/> 88.28	> 26	<0.001/ NA	NA	Rogers RT5880
[24]	33×27.5×0.76	2	28 GHz-band	0.4	6.9/87 (at 28 GHz)	> 17	<0.2/> 9.7	NA	TLY-5
[34]	43.6×43.6×0.4	4	27.4–28.6	1.2	7.9/> 96	> 20	<7×10 ⁻⁴ /> 9.99	<1.2/ NA/ <- 6	Rogers RT5880
[35]	75×110×0.76	4	26–29.5	3.5	9.53/73 (at 28 GHz)	> 22	<0.005/> 9.75	<0.4/ NA/ NA	Rogers RO4350B
[36]	12×25.4×0.8	2	26.83–33.13	6.3	6.4/NA	> 14	<0.005/ > 9.5	NA	Rogers RT5880
[37]	NA	2	26.25–30.14	3.89	5.83/> 80	> 30	<0.005/ > 9.99	<0.4/ NA/ NA	Rogers RO4003
[38]	20×20×2.8	2	27.25–28.59	1.34	9/ NA	> 24	<0.013/> 9.9	NA/> 10/ <-5	Rogers RT5880
[39]	24×24×0.8	4	24.8–44.45	19.65	8.5/> 85	> 18	<0.008/> 9.5	NA	Rogers RT5880
[40]	135×75×0.8	2	27.5–31	3.5	10/NA	> 20	<0.015/> 9.99	<0.4/ NA / <0	Rogers RT5880
[41]	120×60×0.5	2	27.8–28.3	0.5	8.2/> 85	> 25	<0.014/> 9.99	NA/NA/ <-7	Rogers RO4350
[42]	20×20×0.254	2	27.9–28.5	0.6	4.5/NA	> 30	<0.055/> 9.91	NA/NA/ <-10	Rogers RT5880
[43]	11×21.7×0.254	2	25.5–27.79	2.29	5/> 90	> 30	<0.122/> 9.91	<0.5/NA/ <-10	Rogers RT5880
This work	11×20.5×0.254	2	24–34	10	5.9/> 98.7	> 25	<0.036/> 9.99	<0.4/11.25/ <-10	Rogers RT5880
	24×24×0.254	4	24–34	10	7.62/> 98.2	> 22.5	<0.09/> 9.96	NA	RT5880
	39×44.2×0.254	8	24–34	10	8.6/> 98	> 21	<0.14/> 9.91	NA	

The bold line is just used to highlight our results compered to the other references

6 Conclusion

In this paper, a broadband two-port MIMO antenna design has been wisely studied for the utilization in the 5G applications at the mm-wave spectrum. The suggested design

was distinguished by a compact, straightforward and small layout with a total size of 11 × 20.5 × 0.254mm³, operated at 28GHz with a large operating band of 10GHz using the appropriate geometrical modifications. The single-antenna element was marked by a stable radiation pattern throughout the full operating band with a maximum

gain reaching 5.9 dB and high radiation efficiency up to 99%. During this study, we have endeavored to propose a highly isolated UWB MIMO antenna system without enlarging the overall physical area or compromising the design simplicity and the radiation characteristics. This aim was successfully realized using polarization diversity, leading to provide self-decoupled elements where the isolation surpassed 25 dB without introducing any decoupling structure. Thus, a high diversity performance and high channel capacity have been proven by the MIMO antenna where the examined parameters, i.e., ECC, TARC, DG, CCL and CC are all respecting the agreed criteria along the entire operating band. The single and MIMO antennas have been fabricated and tested to validate the simulation results where a good concurrence was achieved. Additionally, the suggested two-port MIMO antenna has been easily expanded to four-port and eight-port MIMO antennas. Both designs exhibited an attractive functionalities while keeping a tiny volumes, which was guaranteed by inserting a simply designed efficacious isolating structures. A detailed comparison with the other previous works has been carried out to emphasize the robustness and the ability of the suggested design to provide a high performance allowing it to be a suitable candidate and highly appropriate for the employment in the 5G systems.

Funding No funding was received for the submitted work.

Data availability statement All data generated or analyzed during this study are included in the manuscript. There is no separated data.

Declarations

Conflict of interest The authors declare no conflicts of interests.

Ethics approval The approval was assured by all authors.

Consent to participate The approval was assured by all authors.

Consent for publication All the authors have given the permission for the publication of this manuscript.

References

- W. Ali, S. Das, H. Medkour, S. Lakrit, Planar dual-band 27/39 ghz millimeter-wave mimo antenna for 5G applications. *Microsyst. Technol.* **27**(1), 283–292 (2021). <https://doi.org/10.1007/s00542-020-04951-1>
- M. Nabil, M.M.A. Faisal, Design, simulation and analysis of a high gain small size array antenna for 5g wireless communication. *Wireless Pers. Commun.* **116**(4), 2761–2776 (2021). <https://doi.org/10.1007/s11277-020-07819-9>
- B. Aghoutane, S. Das, H. Faylali El, B.T.P. Madhav, M. Ghzaoui El, A. Alami El, Analysis, design and fabrication of a square slot loaded (ssl) millimeter-wave patch antenna array for 5g applications. *J Circuits, Syst Comput* **30**(05), 2150086 (2021). <https://doi.org/10.1142/S0218126621500869>
- W. Hong, Z.H. Jiang, Y. Chao, J. Zhou, P. Chen, Y. Zhiqiang, H. Zhang, B. Yang, X. Pang, M. Jiang et al., Multibeam antenna technologies for 5g wireless communications. *IEEE Trans Antennas Propag* **65**(12), 6231–6249 (2017). <https://doi.org/10.1109/TAP.2017.2712819>
- M. Anas, H. Shahid, A. Rauf, A. Shahid, Design of ultra-wide tetra band phased array inverted t-shaped patch antennas using dgs with beam-steering capabilities for 5g applications. *Int. J. Microw. Wirel. Technol.* **12**(5), 419–430 (2020). <https://doi.org/10.1017/S1759078719001594>
- J.G. Andrews, S. Buzzi, W. Choi, S.V. Hanly, A. Lozano, A.C.K. Soong, J.C. Zhang, What will 5g be? *IEEE J Select Areas Commun* **32**(6), 1065–1082 (2014). <https://doi.org/10.1109/JSAC.2014.2328098>
- D.A. Sehrai, M. Abdullah, A. Altaf, S.H. Kiani, F. Muhammad, M. Tufail, M. Irfan, A. Glowacz, S. Rahman, A novel high gain wideband mimo antenna for 5g millimeter wave applications. *Electronics* **9**(6), 1031 (2020). <https://doi.org/10.3390/electronic9061031>
- S.F. Jilani, Q.H. Abbasi, M.A. Imran, A. Alomainy, *Design and analysis of millimeter-wave antennas for the fifth generation networks and beyond*. Wiley 5G Ref: the essential 5G reference online (Wiley, Hoboken, 2019)
- S.F. Jilani, A. Alomainy, Millimetre-wave t-shaped mimo antenna with defected ground structures for 5g cellular networks. *IET Microw Antennas Propag* **12**(5), 672–677 (2018). <https://doi.org/10.1049/iet-map.2017.0467>
- J. Choi, J. Park, Y. Youn, W. Hwang, H. Seong, Y.N. Whang, W. Hong, Frequency-adjustable planar folded slot antenna using fully integrated multithrow function for 5g mobile devices at millimeter-wave spectrum. *IEEE Trans Microw Theory Tech* **68**(5), 1872–1881 (2020). <https://doi.org/10.1109/TMTT.2019.2961088>
- Y. Ghazaoui, A. El Alami, M. El Ghzaoui, S. Das, D. Barad, S. Mohapatra, Millimeter wave antenna with enhanced bandwidth for 5g wireless application. *J. Instrum.* **15**(01), T01003 (2020). <https://doi.org/10.1088/17480221/15/01/T01003>
- M.M. Kamal, S. Yang, S.H. Kiani, D.A. Sehrai, M. Alibakhshikenari, M. Abdullah, F. Falcone, E. Limiti, M. Munir, A novel hook-shaped antenna operating at 28 ghz for future 5g mmwave applications. *Electronics* **10**(6), 673 (2021). <https://doi.org/10.3390/electronics10060673>
- R. Przesmycki, M. Bugaj, L. Nowosielski, Broadband microstrip antenna for 5g wireless systems operating at 28 ghz. *Electronics* **10**(1), 1 (2021). <https://doi.org/10.3390/electronics10010001>
- H. Ullah, F.A. Tahir, A high gain and wideband narrow-beam antenna for 5g millimeter-wave applications. *IEEE Access.* **8**, 29430–29434 (2020). <https://doi.org/10.1109/ACCESS.2020.2970753>
- S. Rangan, T.S. Rappaport, E. Erkip, Millimeter-wave cellular wireless networks: potentials and challenges. *Proc of the IEEE.* **102**(3), 366–385 (2014). <https://doi.org/10.1109/JPROC.2014.2299397>
- S.K. Gupta, A. Bage, A compact, dual-band antenna with defected ground structure for 5g applications. *J Circuits Syst Comput* **30**(16), 150298–150301 (2021). <https://doi.org/10.1142/S0218126621502984>
- M.N. Hasan, S. Bashir, S. Chu, Dual band omnidirectional millimeter wave antenna for 5g communications. *J Electromagn Waves Appl.* **33**(12), 1581–1590 (2019). <https://doi.org/10.1080/09205071.2019.1617790>
- A.A.R. Saad, H.A. Mohamed, Printed millimeter-wave mimo based slot antenna arrays for 5g networks. *AEU Int J Electron*

- Commun **99**, 59–69 (2019). <https://doi.org/10.1016/j.aeue.2018.11.029>
19. C.L. Bamy, F.M. Mbango, D.B.O. Konditi, P.M. Mpele, A compact dual-band dolly-shaped antenna with parasitic elements for automotive radar and 5g applications. *Heliyon* **7**(4), e06793 (2021). <https://doi.org/10.1016/j.heliyon.2021.e06793>
 20. M. Khalid, S.I. Naqvi, N. Hussain, M.U. Rahman, S.S. Mirjavadi, M.J. Khan, Y. Amin et al., 4-port mimo antenna with defected ground structure for 5g millimeter wave applications. *Electronics* **9**(1), 71 (2020). <https://doi.org/10.3390/electronics9010071>
 21. D.A. Sehrai, M. Asif, N. Shoaib, M. Ibrar, S. Jan, M. Alibakhshikenari, A. Lalbakhsh, E. Limiti, Compact quad-element high-isolation wideband mimo antenna for mm-wave applications. *Electronics* **10**(11), 1300 (2021). <https://doi.org/10.3390/electronics10111300>
 22. H.M. Marzouk, M.I. Ahmed, A.H.A. Shaalan, Novel dual-band 28/38 ghz mimo antennas for 5g mobile applications. *Prog Electromagn Res C* **93**, 103–117 (2019). <https://doi.org/10.2528/PIERC19032303>
 23. E.A. Abbas, M. Ikram, A.T. Mobashsher, A. Abbosh, Mimo antenna system for multi-band millimeter-wave 5g and wideband 4g mobile communications. *IEEE Access* **7**, 181916–181923 (2019). <https://doi.org/10.1109/ACCESS.2019.2958897>
 24. M. Usman, E. Kobal, J. Nasir, Y. Zhu, Yu. Chao, A. Zhu, Compact siw fed dual-port single element annular slot mimo antenna for 5g mmwave applications. *IEEE Access* **9**, 91995–92002 (Jun. 2021). <https://doi.org/10.1109/ACCESS.2021.3091835>
 25. C.A. Balanis, *Antenna theory: analysis and design* (Wiley, Hoboken, 2015)
 26. F. Amin, R. Saleem, T. Shabbir, M. Bilal, M.F. Shafique et al., A compact quad-element uwb-mimo antenna system with parasitic decoupling mechanism. *Appl Sci* **9**(11), 2371 (2019). <https://doi.org/10.3390/app9112371>
 27. Y. Lu, Y. Huang, H.T. Chattha, P. Cao, Reducing ground-plane effects on uwb monopole antennas. *IEEE Antennas Wireless Propag Lett* **10**, 147–150 (2011). <https://doi.org/10.1109/LAWP.2011.2119459>
 28. M. Alibakhshikenari, F. Babaeian, B.S. Virdee, S.A. Issa, L. Azpilicueta, C.H. See, A.A. Althuwayb, I. Huynen, R.A. Abd-Alhameed, F. Falcone et al., A comprehensive survey on “various decoupling mechanisms with focus on metamaterial and metasurface principles applicable to sar and mimo antenna systems.” *IEEE Access* **8**, 192965–193004 (2020). <https://doi.org/10.1109/ACCESS.2020.3032826>
 29. A.K. Dwivedi, A. Sharma, A.K. Singh, V. Singh, Design of dual band four port circularly polarized mimo dra for wlan/wimax applications. *J Electromagn Waves Appl* **34**(15), 1990–2009 (2020). <https://doi.org/10.1080/09205071.2020.1801522>
 30. A.K. Dwivedi, A. Sharma, A.K. Pandey, V. Singh, Two port circularly polarized mimo antenna design and investigation for 5g communication systems. *Wireless Pers Commun* (2021). <https://doi.org/10.1007/s11277-021-08461-9>
 31. G. Varshney, S. Gotra, V.S. Pandey, R.S. Yaduvanshi, Proximity-coupled two-port multi-input-multi-output graphene antenna with pattern diversity for thz applications. *Nano Commun Netw* **21**, 100246 (2019). <https://doi.org/10.1016/j.nancom.2019.05.003>
 32. A. Kumar, A.Q. Ansari, B.K. Kanaujia, J. Kishor, A novel it-shaped isolation structure placed between two-port cpw-fed dual-band mimo antenna for high isolation. *AEU Int J Electron Commun* **104**, 35–43 (2019). <https://doi.org/10.1016/j.aeue.2019.03.009>
 33. A. Khabba, S. Errahili, S. Ibnyaich, A. Zeroual (2021) A new 2 × 2mimo trapezoidal shaped antenna with high gain and wide bandwidth for 37–40 GHz millimeter wave applications. In *Proceedings of the 4th International Conference on Networking, Information Systems Security*. <https://doi.org/10.1145/3454127.3456584>
 34. B. Aghoutane, S. Das, M. El Ghzaoui, B.T.P. Madhav, H. El Faylali, A novel dual band high gain 4-port millimeter wave mimo antenna array for 28/37 ghz 5g applications. *AEU Int J Electron Commun* **145**, 154071 (2022). <https://doi.org/10.1016/j.aeue.2021.154071>
 35. S.I. Naqvi, N. Hussain, A. Iqbal, M. UrRahman, M. Forsat, S.S. Mirjavadi, Y. Amin, Integrated LTE and millimeter-wave 5G mimo antenna system for 4G/5G wireless terminals. *Sensors* **20**(14), 3926 (2020). <https://doi.org/10.3390/s20143926>
 36. M. Venkateswara Rao, B.T.P. Madhav, J. Krishna, Y. Usha Devi, T. Anilkumar, B. Prudhvi Nadh, Csrr-loaded t-shaped mimo antenna for 5g cellular networks and vehicular communications. *Int J RF Microw Comput-Aided Eng* **29**(8), e21799 (2019). <https://doi.org/10.1002/mmce.21799>
 37. H. Zahra, W.A. Awan, W.A.E. Ali, N. Hussain, S.M. Abbas, S. Mukhopadhyay, A 28 Ghz broadband helical inspired end-fire antenna and its mimo configuration for 5g pattern diversity applications. *Electronics* **10**(4), 405 (2021). <https://doi.org/10.3390/electronics10040405>
 38. Y. Zhang, J.-Y. Deng, M.-J. Li, D. Sun, L.-X. Guo, A mimo dielectric resonator antenna with improved isolation for 5G mm-wave applications. *IEEE Antennas Wirel. Propag. Lett.* **18**(4), 747–751 (2019). <https://doi.org/10.1109/LAWP.2019.2901961>
 39. A. Patel, A. Desai, I. Elfergani, A. Vala, H. Mewada, K. Mahant, S. Patel, C. Zebiri, J. Rodriguez, E. Ali, UWB CPW fed 4-port connected ground MIMO antenna for sub-millimeter-wave 5G applications. *Alex. Eng. J.* **61**(9), 6645–6658 (2022). <https://doi.org/10.1016/j.aej.2021.12.015>
 40. S.M. El-nady, A.M. Attiya, Periodically-stub-loaded microstrip line wideband circularly polarized millimeter wave MIMO antenna. *IEEE Access* **10**, 20465–20472 (2022). <https://doi.org/10.1109/ACCESS.2022.3152222>
 41. R. Hussain, M. Abou-Khousa, N. Iqbal, A. Algarni, S.I. Alhuwaimel, A. Zerguine, M.S. Sharawi, A multiband shared aperture MIMO antenna for millimeter-wave and sub-6GHz 5G applications. *Sensors* **22**(5), 1808 (2022). <https://doi.org/10.3390/s22051808>
 42. D. Sharma, R. Katiyar, A.K. Dwivedi, K.N. Nagesh, A. Sharma, P. Ranjan, Dielectric resonator-based two-port filterennas with pattern and space diversity for 5G IoT applications. *Int J Microw Wireless Technol* (2022). <https://doi.org/10.1017/S1759078722000150>
 43. A. Kumar, A.K. Dwivedi, K.N. Nagesh, A. Sharma, P. Ranjan, Circularly polarised dielectric resonator based two port filterenna for millimeter-wave 5G communication system. *IETE Tech Rev* (2022). <https://doi.org/10.1080/02564602.2022.2028588>

Publisher's Note Springer Nature remains neutral with regard to jurisdictional claims in published maps and institutional affiliations.

Springer Nature or its licensor holds exclusive rights to this article under a publishing agreement with the author(s) or other rightsholder(s); author self-archiving of the accepted manuscript version of this article is solely governed by the terms of such publishing agreement and applicable law.